Numerical simulation of ice crystal icing in an axial compressor rig

Tristan Soubrié, Moussa Diop, Claire Laurent, Maxime Bouyges, Jean-Mathieu Senoner, Philippe Villedieu, Martin O Neuteboom

Numerical simulation of ice crystal icing in an axial compressor rig

Tristan Soubrié*, Moussa Diop†
ANDHEO, F-92320 Châtillon, France

Claire Laurent‡, Maxime Bouyges§, Jean-Mathieu Senoner¶ and Philippe Villedieu‖
ONERA / Université de Toulouse, F-31055 Toulouse, France

Martin O. Neuteboom**
National Research Council of Canada, Ottawa, Ontario, K1A 0R6, Canada

Numerical simulations of ice crystal icing within an experimental single-stage compressor test rig representative of realistic aeronautical engines are investigated. This paper aims to assess the icing models in CEDRE multi-physics CFD code recently developed and implemented. Gas flow, ice crystal trajectories, fragmentation dynamics and melting along the geometry are successively computed before the ice accretion in the test article is calculated using a surfacic solver that includes recently developed erosion and porosity models. Three experimental operating points are considered, with wet bulb temperatures increasing from negative to positive values and respectively exhibiting no accretion, significant accretion and moderate accretion. The comparison of simulation results with experiments for these cases shows a good agreement in terms of occurrence, location and surfacic extension of accretion phenomena. Nevertheless, a global shift in the inlet temperature is necessary to reproduce experimental results.

I. Nomenclature

Dv50	=	Median volumetric diameter
Dvxx	=	Diameter delimiting xx% of the particle volume distribution
ICE-MACR	=	Ice Crystal Environment Modular Axial Compressor Rig
ICI	=	Ice crystal icing
OGV	=	Outlet guide vanes

*Director
†Reseach engineer
‡Research Engineer, DMPE-MH
§Research Engineer, DMPE-MH
¶Research Engineer, DMPE-MH
‖Research Director, DMPE
**Research Officer

Pstat	=	Static pressure
P0	=	Total pressure
RH	=	Relative humidity compared to vapor saturation, in %
Tstat	=	Static temperature
T0	=	Total temperature
Twb	=	Wet bulb temperature based on static pressure and temperature
Twb0	=	Wet bulb temperature based on total pressure and temperature
TWC	=	Total water content

II. Introduction

Aircraft engines flying in cold conditions are often submitted to icing. This is of two kinds: icing caused by supercooled liquid droplets and ice crystal icing. The first type has been reported to appear on external airplane surfaces or aircraft engine compressors since the 1920s [1] and is often accompanied by a considerable reduction in aerodynamic performances [2]. This mode of icing is well known and several numerical tools are available to predict its formation. More recently, ice crystal icing has been found to be responsible for several in-service events (probe blockage, engine rollbacks, and flameouts) when flying at high altitudes in tropical regions through clouds with high ice-crystal concentrations (ranging in size from 50 µm to 1 mm) or with mixed phase conditions, i.e., ice crystals combined with supercooled water droplets. A report [3] identified over 140 engine power loss events due to engine core icing since the early 1980s. The mode of ice crystal accretion is as follows: ice particles entering warm airplane parts (compressor, heated probes equipped with anti-icing or de-icing systems) are partially melted, which increases their sticking capability on solid surfaces. The icing of external probes may lead to probe inlet obstruction in case of severe icing conditions causing erroneous measurements.

Icing is a significant safety concern for the aeronautic industry since it can lead to dramatic events [4, 5]. Therefore, to improve the safety of airplane flights, new certification rules were defined for flying in ice-crystal icing conditions. ICI is extremely difficult and expensive to reproduce experimentally (ice crystal concentration and size distribution, flight altitude pressure, speed, and temperature) at the ground level on full-scale engines. Currently, this kind of icing is not fully addressable with numerical tools either. Consequently, scientific efforts have focused on this issue in order to provide the aeronautical industry with multi-physics numerical simulation tools, to help the aeronautic industry to assess ice crystal icing on the next generation of air data probes and future generations of aircraft engines designed with high bypass ratio, and meet certification requirements. These future generations of products are designed to be more energy efficient: engines with high bypass ratio could lead to an increase of ingested particles, and air probes data with low energy consumption may imply reduced heat power for de-icing systems. Therefore, they will probably be more

susceptible to ICI than currently in-service turbofan and air data probes.

Due to the complexity of current aircraft engine architectures, validation of the numerical tools on simplified yet representative configurations appears as a crucial step to reach this objective. The Ice Crystal Environment Modular Axial Compressor Rig (ICE-MACR) [6] is an appropriate candidate since it has been designed to simulate ice crystal ingestion into an engine compressor at in-flight conditions. Neuteboom *et al.* [7–11] have reported several test campaigns started in 2019 with measurements including gas pressure, temperature and relative humidity, particle size and concentration distributions, as well as pictures exhibiting accretion on a test article. Nilamdeen *et al.* [12] performed computations using Ansys numerical simulation suite to model ICI in the ICE-MACR for two test cases referred as #133.01 and #135.01. They used the Eulerian finite-element solver FENSAP-ICE to compute ice crystal dynamics and possible accretion. Not only initial impingement on walls but also secondary, although numerically limited, particle entrainment back into the flow domain are modelled. However, particle breakup on walls as well as particle size distribution are not accounted for. As a consequence, the Mean Volume Diameter is used to inject a single sized ice-crystal at the test facility inlet while post-break-up diameters are defined as an inlet boundary condition for diameter downstream the rotor. Despite those limitations, accretion in the test article could be simulated and has shown, for one test point, agreement with the experiments regarding the occurence, location and extent of the accretion, while for the other test point the simulation predicts accretion whereas the experiment does not show any.

The current work deals with the numerical simulation of ice crystal dynamics and accretion within the ICE-MACR using Cedre platform [13]. Ice crystal dynamics is computed using a Lagrangian approach, accounting for particle size distribution and breakup on walls. Accretion is computed using a dedicated surfacic solver. First, gas flow, ice crystal trajectories, and the associated fragmentation dynamics within the compressor stage are investigated for different rotor speeds. For this purpose, numerical simulations with two different fragmentation models are compared for cold conditions, i.e., with a sufficiently negative wet bulb temperature to ensure fully glaciated particles. The comparison between the fragmentation models aims at assessing the capabilities of a recently proposed ice crystal fragmentation model with respect to a state-of-the-art model. In a second step, several experimental operating points with wet bulb temperatures rising from negative to positive values are simulated. The points thus exhibit no melting, moderate melting, and significant melting respectively, leading to various severity levels in terms of accretion. The results of numerical simulations are described in details and compared to available experimental data and observations. The discrepancies are extensively analysed and their origins seeked for, in order to provide a basis for future improvement in model fidelity to predict ICI.

III. ICE-MACR Experiment set-up

ICE-MACR is a modular axial compressor test rig designed to simulate ice crystal ingestion into an engine compressor at flight conditions. The setup considered in the present study is shown in Fig. 1. It consists of a single

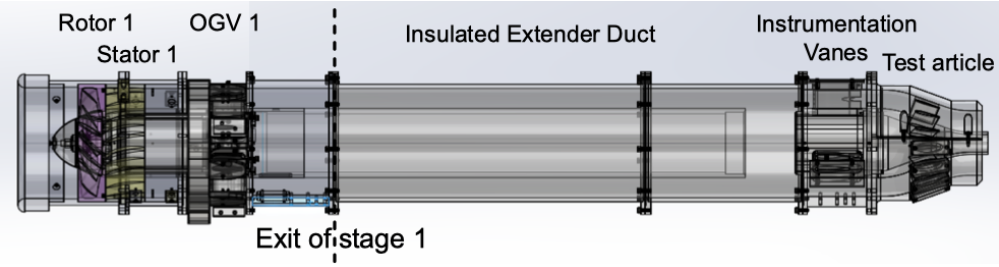

Fig. 1 ICE-MACR module concept in single stage accretion configuration.

compressor stage comprising a rotor, a stator, and an array of uncambered NACA 0018 outlet guide vanes (OGV's). An extender duct is placed downstream of the compressor stage in order to enhance ice particle melting. The extender duct is followed by the instrumentation segment to characterize ice crystal properties. It consists of three hollow NACA 0018 struts. The struts contain a rear-facing camera to record accretion, the particle detection probe array, which measures a radial distribution of particles and their passing velocity, a relative humidity probe, a total pressure tap, and leading-edge thermocouples to measure total temperature. The outer casing of the instrumentation segment holds a pressure tap to measure static pressure. The inner casing of the instrumentation segment includes a radially aligned camera to observe accretion on the outer casing wall. Finally, a test article consisting of a swan neck duct with guide vanes similar to an inter-compressor duct completes the setup. The test article comprises a 20-degree converging annulus with 15 uncambered NACA 0012 airfoils. The hub and part of the outer shell are semi-transparent. Two borescope cameras pointing radially outwards are installed in the hub, one in line with the airfoil leading edge plane and one in line with the airfoil trailing edge plane. The overall length of the present ICE-MACR setup is 1.3 m with a casing inner diameter of 145 mm.

Accretion experiments were performed by injecting ice particles into the wind tunnel settling chamber upstream of the rig at altitude conditions. A sweep of the accretion plateau was obtained by varying the tunnel total temperature T0 from cold c. $-10\,^{\circ}$C to just below $0\,^{\circ}$C. Accretion was observed via embedded borescope cameras within the test article and instrumentation segment for inlet total temperature ranging from $-7\,^{\circ}$C to $-2\,^{\circ}$C. Accretion behaviour was qualitatively categorized into severity levels which were graded in order of their potential threat to safe operability of an aircraft engine. Melt ratio measurements were made using SEA T multi-element probe which has two hot wire elements, one which records liquid water content and another which records total water content. In order to make melt ratio measurements, the test article was removed and replaced with a dummy cone which creates back pressure while permitting the T-MEP to be inserted. T0 was then varied and melt ratio measured. Melt ratio was then correlated to total wet bulb temperature Twb0 at the test article inlet. For the accretion runs, the melt ratio was determined by substituting the Twb0 measured during an accretion run into the melt-ratio - Twb0 correlations. For particle break-up measurements, the extender duct was removed and the same dummy cone used with the multi-wire probe melt ratio measurements was

installed immediately downstream of stage 1. The shadowgraph then imaged particles as rotor speed was varied via cut-outs at the top and bottom of the dummy cone [7].

IV. Simulation tool

The CFD code CEDRE [13] is used in the present study. It is a multi-solver platform dedicated to both steady and unsteady flow simulations. In the present computations, three solvers are used: the CHARME solver to simulate the aerodynamic flow field, the SPARTE solver to compute the ice particle trajectories in a Lagrangian framework, and the FILM solver to predict ice accretion on walls.

A. Gas solver

The aerodynamic flow solver CHARME solves the Reynolds Averaged Navier-Stokes (RANS) equations for a gas mixture of two species, namely air, and water. The $k-\omega$ turbulence model of Menter with SST correction is used [14]. Time integration is performed with an implicit first-order Euler scheme associated with a Generalized Minimal RESidual (GMRES) method to solve the linear system. Local time stepping is used to ensure numerical stability while accelerating convergence. The convective fluxes are calculated with a 2nd order Monotonic Upwind Scheme for Conservation Laws (MUSCL) [15] method and a Harten-Lax-van Leer-Contact (HLLC) scheme [16].

To account for the presence of moving parts in the geometry (rotor), the momentum equations are solved in a rotating frame of reference while maintaining the geometry fixed. Such description yields additional volumetric forces, namely Coriolis and centrifugal forces. The conversion from fixed to rotating frames of reference is then handled via mixing planes. Mixing planes are also used to reduce the computational domain to one blade passage per row and handle the cross-section variations from one sector size to another.

Steady computations are performed. Convergence is checked in particular on flow rates, with fluctuations below 0.1%.

B. Lagrangian particle solver

The SPARTE Lagrangian particle solver is used to compute ice-crystal trajectories and heat exchange phenomena with gas-phase within the test rig.

The Lagrangian dispersed phase approach is based on a direct resolution of the Boltzmann-type equation describing the evolution of the particle density function [17] (spray density function in the nomenclature used in [17]). Its evolution is then computed by approximating the particle density function as a sum of Dirac delta functions centered on each particle sample. This approach allows for a straightforward implementation of physical models and natural handling of polydispersity. On the contrary, the Lagrangian approach suffers from poor accuracy in regions of low particle density.

The Lagrangian particle solver is described in five parts: numerical algorithm, particle otion, particle mass and heat

transfer phenomena, wall impingement, mixing plane. The interested reader may find further details on most of these aspects in [18]

1. Numerical algorithm

The present simulations are steady in the sense that particle trajectories are computed using an averaged flow field for the fluid carrier phase. In addition, two-way coupling effects (e.g., flow field perturbations induced by the particles) are not taken into account. Numerical particles are injected once at the inlet, and their trajectories are calculated until they all exit the computational domain, either through the outlet, by entirely sticking on walls, or through full evaporation. The evaluation of interphase exchange phenomena between particle and gas requires the evaluation of gas properties at the particle position. The latter are reconstructed at the particle's center of gravity using linear interpolation within the computational cell where the particle is located. The localization of the particles on the Eulerian grid is performed using an algorithm proposed by Hasselbacher [19].

2. Particle motion

Particle motion is influenced by drag, gravity, added mass and Basset history forces [20, 21]. At high particle to air density ratios (of the order of one thousand) and small particle sizes (less than a few hundred microns), dimensional analysis indicates that drag is largely predominant over all other forces. The expression for particle momentum may thus be written as:

$$m_p \frac{d\vec{u}_p}{dt} = \frac{\pi}{8} \rho_a d_p^2 C_D \left|\vec{u}_a - \vec{u}_p\right| \left(\vec{u}_a - \vec{u}_p\right) \tag{1}$$

An analytical expression for drag is only known for particle Reynolds numbers that are small compared to unity. However, most practical applications involve finite particle Reynolds numbers, so empirical correlations are required to close the drag term. In addition, ice crystals display shapes that are generally not spherical; thus, corrections accounting for deviation from sphericity need to be included. In the present case, a correlation proposed by Ganser for isometric particles is used to evaluate the drag coefficient C_D [22]. The latter depends on the particle sphericity ϕ, defined as the ratio of the surface area of a sphere with the same volume as the particle and the projected surface area A of that particle, i.e., $\Phi = \pi d_p^2 / A$.

3. Particle mass and heat transfer phenomena

Three distinct phase-change processes may occur along particle trajectories: sublimation, fusion (melting), and evaporation. These three phase changes are driven by diffusive mass and heat transfer phenomena between the particles and the surrounding gas.

Particle mass transfer is modeled using Spalding's evaporation model [23]:

$$\frac{dm_p}{dt} = -\pi d_p \frac{\mathrm{Sh}}{\Phi} \rho_a D_v \ln\left(1 + B_M\right) \tag{2}$$

with B_M the Spalding mass transfer number:

$$B_M = \frac{y_{v,s} - y_{v,a}}{1 - y_{v,s}} \tag{3}$$

with $y_{v,s}$ and $y_{v,a}$ respectively denote the vapor mass fraction at the particle surface and outside the vapor layer surrounding the particle. Depending on the particle state, which is deduced from its temperature, the mass source term given by the right-hand side of eq. 2 either represents evaporation (partially/fully melted) or sublimation (fully solid).

Heat transfer phenomena at the particle-air interface are driven by heat conduction and the enthalpy variation due to phase change:

$$m_p c_{p,p} \frac{dT_p}{dt} = \pi d_p \frac{\mathrm{Nu}}{\Phi} k_a \frac{\ln\left(1 + B_T\right)}{B_T} \left(T_a - T_p\right) - \dot{m}_p L \tag{4}$$

As for eq. 2, the specific heat capacity at constant pressure $c_{p,p}$ of the particle and the latent heat of phase change L need to be modified according to the particle state, i.e., solid for sublimation, partially/fully melted for evaporation. The Spalding heat transfer number writes:

$$B_T = \left(1 + B_M\right)^{\delta} - 1 \tag{5}$$

with:

$$\delta = \frac{c_{p,v}}{c_{p,g}} \frac{\mathrm{Sh}}{\mathrm{Nu}} \frac{1}{\mathrm{Le}_v} \tag{6}$$

with $c_{p,v}$, $c_{p,g}$ respectively the heat capacity of the pure vapor species and the gas mixture in the vicinity of the particle, while $\mathrm{Le}_v = \mathrm{Sc}_v / \mathrm{Pr}_v$ represents the Lewis number of the vapor species. The expressions used for Sherwood Sh and Nusselt Nu numbers, as well as the modeling for the variation of sphericity Φ are detailed in [24].

4. Wall impingement

The interaction of a (potentially partially melted) ice crystal with a wall is a complex process. The main parameters influencing impact outcomes and dynamics are particle size, impact velocity, and melting ratio. In the present work, the two first parameters are included in the impact model itself, while the third parameter is assumed to solely control the deposited masses of solid and liquid.

Two different impact models are compared in the present work. The comparison aims to assess their respective capabilities in an engine under the same conditions. The first model was proposed within the European HAIC project [24] and will be referred to as 'HAIC' model in the following. The second model differs only regarding the description

of the fragmentation regime. It was derived within the European MUSIC-haic project to incorporate basic physical principles between fragmentation's initial and end states. It will be designated 'MUSIC-haic' model in the following. More details on the MUSIC-haic model may be found in [25].

Both models rely on the same thresholds for the different impact regimes. The classification of impact outcomes is based on the Vidaurre number [26], which represents a ratio of the particle's kinetic energy upon impact (driving fragmentation) with its surface energy (ensuring the particle's cohesion):

$$\mathcal{L} = \frac{\rho_p d_p u_{p,n}^2}{12 e_\sigma} \tag{7}$$

The surface energy of ice is temperature dependent and expressed as

$$e_\sigma(T) = e_{\sigma 0} \exp\left[\frac{Q_s}{R}\left(\frac{1}{T_p} - \frac{1}{T_0}\right)\right]. \tag{8}$$

Vidaurre and Hallett [26] evaluate the initial surface energy as $e_{\sigma 0} = 0.12\,\mathrm{J\,m^{-2}}$ at the reference temperature $T_0 = 253\,\mathrm{K}$.

The classification of impact outcomes established by Trontin *et al.* [24] is used:

$\mathcal{L} < \mathcal{L}_1$	elastic particle bouncing
$\mathcal{L}_1 < \mathcal{L} \leq \mathcal{L}_2$	inelastic particle bouncing
$\mathcal{L} > \mathcal{L}_2$	particle fragmentation

with $\mathcal{L}_1 = 0.5$ and $\mathcal{L}_2 = 90$.

In the two first regimes, the particle diameter remains unchanged: while internal cracks may form in the second regime, the particle is assumed to remain intact. The difference between both regimes then lies in the damping of the incoming normal velocity component ξ. On the contrary, the particle is assumed to shatter in the third regime. The associated size reduction is expected to favor melting, and accurate modeling of fragmentation dynamics is thus essential to predict the occurrence of icing.

Regarding the fragments' size characteristics, the HAIC model relates the maximum diameter of the reemitted fragments to the Vidaurre number via a power law :

$$d_{p,max} = \left(\frac{\mathcal{L}_2}{\mathcal{L}}\right)^{2/11} d_p \tag{9}$$

Based on the analysis of several experimental databases [25], the MUSIC-haic model derives the size of the largest ice particle fragments within the energy horizon framework proposed by Grady [27]. The latter is based on an energy conservation principle between fragmentation's initial and end states. The maximum diameter may then be related to

the characteristic strain rate $\dot{\varepsilon}$ resulting from impact:

$$\frac{d_{p,max}}{s_0} = C_f \left(\frac{\dot{\varepsilon}}{\dot{\varepsilon_0}} \right)^{\alpha} \tag{10}$$

with s_0 and $\dot{\varepsilon_0}$ normalization parameters [28] while C_f and α represent the adjustment parameters of the underlying semi-empirical model. Finally, it is assumed that the indentation radius formed upon impact defines the tensile strain levels, which eventually cause the particle to shatter. Thus, the strain rate estimate is based on the indentation radius formed upon impact [29, 30] and scales as:

$$\dot{\varepsilon} \sim u_{p,n}^{1/2} d_p^{-1} \rho_p^{-1/4} Y_c^{1/4} \tag{11}$$

with $Y_c = 5.2 \times 10^6$ Pa a reference value for the compressive yield strength of ice. A regression fit to a large experimental dataset then yields $C_f \approx 23.936$ and $\alpha \approx -0.896$. It appears that the improvement regarding the prediction of the maximum fragment diameter with respect to experiments is moderate from the HAIC to the MUSIC-haic model, with average error levels being reduced by a few percent with respect to available experimental data [25].

The MUSIC-haic model assumes a power law distribution on the fragment number density function:

$$p_n(d_p) = \frac{\gamma - 1}{d_{p,max}^{\gamma-1} - d_{p,min}^{\gamma-1}} d_p^{-\gamma} \tag{12}$$

with $\gamma = 2.73$ and $d_{p,min} = 0.015 d_{p,max}$, while $d_{p,max}$ is given by eqs. 10 and 11. No reliable experimental data regarding the size distribution of the reemitted ice fragments were available when the HAIC model was proposed. It was then arbitrarily assumed that the mass distribution after fragmentation was uniform, corresponding to $\gamma = 3$ in eq. 12. Therefore, the size distributions assumed for both models are coincidentally similar as well. Thus, the main advantage of the MUSIC-haic fragmentation model lies in its reduced degree of empiricism compared to the HAIC model, which could allow for further improvements in ice crystal impact modeling.

The sphericity distribution of the fragments appears difficult to model. In addition, experimental data on this parameter seem very scarce. For this reason, the fragments' sphericity is drawn as a uniform random number within the range $\phi \in [0.6; 1.0]$.

Currently, experiments performed within the MUSIC-haic project only yield access to the radial velocity distribution of the reemitted fragments: only the normal velocity of the largest fragment may be measured with the existing experimental setups. For this reason, both models share the same correlations for the normal restitution coefficient ξ_{nn} provided by Trontin *et al.* [24], defined as the ratio of the normal velocity components after and before impact. The

latter is written as:

$$\xi_{nn} = \begin{cases} 1 & \text{if } \mathcal{L} \leq \mathcal{L}_{c1}, \\ \left(\frac{\mathcal{L}_{c1}}{\mathcal{L}}\right)^{1/3} & \text{if } \mathcal{L} > \mathcal{L}_{c1}. \end{cases} \tag{13}$$

Regarding the damping coefficient of the velocity component tangential to the impinged surface, the latter is assumed to equal unity regardless of the impact velocity, i.e., $\xi_t = 1$.

For the HAIC model, the restitution coefficient ξ_{nt} describing the tangential velocity component induced by the normal incoming velocity component in case of fragmentation writes:

$$\xi_{nt} = 0.4\left(1 - \sqrt{\frac{\mathcal{L}_{c2}}{\mathcal{L}}}\right) \tag{14}$$

On the other hand, the MUSIC-haic model interprets this velocity component as resulting from the tensile strain induced upon impact. First, the strain rate given by eq. 11 is interpreted as an average value within the particle. A random distribution of fragments within the original particle given by 12 is then assumed. Finally, the size of a fragment and the location where it forms within the original crystal are assumed decorrelated, i.e. large fragments do not preferentially form towards the center for instance. Expressing eq. 12 in terms of fragment radii r_p instead of diameters for convenience then yields:

$$\begin{aligned} \xi_{nt} &= k\,\frac{1}{u_{p,n}}\int_{r_{p,min}}^{r_{p,max}} \frac{\gamma-1}{r_{p,max}^{\gamma-1} - r_{p,min}^{\gamma-1}} r_f^{-\gamma} \int_0^{r_p - r_f}\int_0^{2\pi}\int_0^{\pi} \frac{1}{4/3\pi(r_p - r_f)^3} k\dot{\varepsilon}(r_p + r\cos\theta) r^2 \sin\theta dr d\theta d\phi dr_f \\ &= k\,\frac{3}{32}\pi u_{p,n}^{-1/2}\rho_p^{-1/4} Y_c^{1/4}\left[1 - \frac{1}{r_p}\frac{r_{p,max}^{2-\gamma} - r_{p,min}^{2-\gamma}}{r_{p,max}^{1-\gamma} - r_{p,min}^{1-\gamma}}\right] \end{aligned} \tag{15}$$

The parameter k is then used to adjust the model to the available experimental data, yielding $k \approx 0.909$.

The sticking efficiency ε_{ic}, defined as the ratio of sticking to impinging mass, is assumed to solely depend on particle melt ratio η_m [24]:

$$\varepsilon_{ic} = (K_{ic} - 2)\eta_m^3 + (3 - 2K_{ic})\eta_m^2 + K_{ic}\eta_m \tag{16}$$

with the melt ratio defined as the ratio of particle liquid to total water content.

5. Mixing plane

Similarly to the gas carrier phase, the particle simulations account for the presence of moving parts by resolving the particle equations of motion in a rotating frame of reference and accounting for Coriolis and centrifugal forces. Fixed and moving reference frames are also connected via mixing plane boundary conditions. The mixing plane interfaces are split into rings in the radial direction. Particle properties are mass averaged over each ring, and mean values are transferred to the corresponding ring on the other side of the mixing plane. New numerical particles are then injected

downstream, with sizes following a log-normal mass distribution that conserves the average upstream diameter and standard deviation. The average melting rate is also conserved per ring, but reinjected particle sizes and melting rates are imposed so as to conserve correlations that may exist between these parameters. The following centred and normalized random numbers are defined for the melting rate and the particle diameter:

$$x_{d_p} = \frac{d_p - \overline{d_p}}{\sigma_{d_p}} \tag{17}$$

$$x_{\eta_m} = \frac{\eta_m - \overline{\eta_m}}{\sigma_{\eta_m}} \tag{18}$$

where $\bar{\cdot}$ denotes a mass average and $\sigma_{\cdot}$ the associated standard deviation of the considered quantity. The associated correlation matrix may then be defined as:

$$\mathbf{C} = \begin{pmatrix} \rho_{d_p d_p} & \rho_{d_p \eta_m} \\ \rho_{\eta_m d_p} & \rho_{\eta_m \eta_m} \end{pmatrix} \tag{19}$$

with for instance:

$$\rho_{d_p \eta_m} = \overline{x_{d_p} x_{\eta_m}} - \overline{x_{d_p}}\,\overline{x_{\eta_m}} = \overline{x_{d_p} x_{\eta_m}} \tag{20}$$

Thus, the diagonal elements are equal to one given the chosen normalization, i.e. $\rho_{d_p d_p} = \rho_{\eta_m \eta_m} = 1$, and the matrix is symmetric by definition.

First, melting ratio and diameters of the reinjected particles are randomly and independently drawn given their means and variances, yielding x_{d_p} and x_{η_m} according to relations 17 and 18. Then, a correlated vector random vector $\mathbf{x_c}$ may be evaluated from the original random vector $\mathbf{x} = \left[x_{d_p}, x_{\eta_m}\right]$ by a simple matrix vector product

$$\mathbf{x_c} = \mathbf{U}\mathbf{x} \tag{21}$$

with $\mathbf{U}$ the upper triangular matrix of $\mathbf{C}$:

$$\mathbf{C} = \mathbf{U}^{\mathbf{T}}\mathbf{U} \tag{22}$$

which may be obtained via Cholesky decomposition. The procedure outlined above is strictly speaking only valid for random numbers following a normal distribution, which is inaccurate in the present case since both the melting ratio and the particle diameter are positive random variables. Nevertheless, this procedure may still be applied by making the more reasonable assumption that both parameters follow a log-normal distribution, i.e., that the logarithms of their mass averages are normally distributed. The only modifications to be applied are to perform the mass averages on the logarithms of these quantities in eqs. 17, 18, 20 and to take the exponential of the resulting correlated random numbers in the final step. However, this transformation does not solve the issue of the unitary upper bound of the melt ratio. For

the moment, the variance of the melt ratio is corrected so that the normalized probability mass distribution based on the melt ratio tends to unity when the melt ratio tends to unity. While it was verified that this correction only induced minor changes in the variance in practice, the current procedure clearly requires further improvements. A solution could consist of using copulas [31] as they seem to provide a framework allowing to draw correlated random numbers using different probability distributions for each variable.

C. Accretion solver

The 3D accretion solver is the FILM surface solver. It uses an integral eulerian approach to solve wall liquid film and accretion equations over a 3D wall surface. The solver was initially developed to simulate water ingestion in turbojet engines (thus containing all functionalities necessary for rotating frames) and has then been upgraded to include a two-layers accretion model for icing simulations [32]. The FILM geometry (a surface mesh) is built from the CEDRE geometry (a general unstructured volume mesh) and it is partitioned for parallel computations. Regarding coupling aspects, the FILM solver is coupled with the gas phase solver CHARME to compute the shear-driven force, the gas pressure gradient acting on the film motion, as well as the heat and the mass transfer coefficients for the calculation of exchanges with the airflow. The source terms for the disperse phase are obtained using either SPIREE, CEDRE's eulerian dispersed solver, or SPARTE, CEDRE lagrangian solver. In the framework of ice crystal accretion, the solver is coupled with SPARTE solver through the sticking efficiency model. Four accretion regimes can be distinguished in ice accretion modeling: full-evaporative regime (dry wall), running wet conditions (only a wall liquid film), rime ice conditions (only ice with a negative temperature) and glaze ice conditions (ice at the wall with a liquid film above). A coupled erosion and porosity model for ICI modeling has been implemented for the glaze ice regime. The following subsections describe these models in more detail.

1. ICI models for glaze ice regime

The glaze ice regime is characterized by an ice layer at the wall with a running liquid film above, both the ice and the film being at the melting temperature T_m. The first step is to compute the mass deposition flows Φ_{dep} from the impingement fluxes Φ_{imp}. Here, the model coming from European HAIC project is used to calculate the sticking efficiency ϵ_S

$$\epsilon_S = (K_C - 2)\eta_m^3 + (3 - 2K_C)\eta_m^2 + K_C\eta_m \tag{23}$$

with $K_C = 2.5$ [33]. Then, a classical "Messinger" balance is carried out to obtain the fusion mass flux Φ_{fus}, corresponding to the phase change between the ice layer and the liquid layer. This is required to obtain the total liquid fraction f_l defined by

$$f_l = \frac{\Phi_{dep,m,l} + \Phi_{rb,in,m,l} + \Phi_{fus} - \Phi_{evap}}{\Phi_{dep,m,s} + \Phi_{dep,m,l} + \Phi_{rb,m,in,l} - \Phi_{evap}} \tag{24}$$

where $\Phi_{dep,m}$ are the mass deposition fluxes, Φ_{evap} the evaporation flux and $\Phi_{rb,in,m,l}$ the liquid runback flux. This liquid fraction f_l is used to split the erosion mass loss between liquid and solid such as

$$\Phi_{er,s} = (1 - f_l)\Phi_{er} \tag{25}$$

$$\Phi_{er,l} = f_l\Phi_{er} \tag{26}$$

However, the total mass erosion flux Φ_{er} depends on the ice porosity, which is assumed to be related to the liquid mass fraction α_l defined by the ratio between the liquid accumulated water* $h_{l,acc}$ and the total accumulated water, both liquid and solid

$$\alpha_l = \frac{\rho_l h_{l,acc}}{\rho_l h_{l,acc} + \rho_s h_s} \tag{27}$$

These quantities are evaluated after the computation of the erosion losses, and consequently, it implies a coupling between the erosion and the porosity models. These two models are described in the following subsections.

2. Erosion model

The semi-empirical model of Charton et al. [34, 35] based on the theoretical considerations on solid-solid impact proposed by Finnie and Bitter [36–38], have been implemented in FILM. In this model, two main mechanisms characterize impact-driven erosion phenomena: deformation and cutting. Erosion occurs when the particle normal velocity V_n is greater than the ice elastic limit velocity V_{el}. The volume eroded by cutting Vol_C and deformation Vol_D enables to compute the erosion flux.

$$\Phi_{er} = F_s\rho_s(Vol_C + Vol_D) \tag{28}$$

where F_s is a sharpness factor depending on the sphericity factor. Detailed expression of Vol_C and Vol_D are given in [35]. In this model, particle diameter's effect on erosion is considered. For this purpose, the energy dissipated by the particle fragmentation is modeled through an "effective" particle velocity. It corresponds to the particle velocity when the energy dissipated by its fragmentation is subtracted from its kinetic energy. As the energy dissipated depends on the damaged volume, the resulting erosion model depends on particle diameter. Finally, the effect of ice porosity is also modeled through correction coefficients on the Young modulus and the elastic limit of ice with respect to the liquid mass fraction α_l.

*The liquid accumulated water is the liquid water trapped in the ice layer.

3. Porosity model

The model for liquid imbibition in porous ice layer implemented in the FILM solver is described in [24]. The maximum amount of accumulated water is a function of the ice porosity Ψ and the liquid deposition fraction ξ_l:

$$h_{l,acc,max} = h_s \frac{\Psi}{1-\Psi}(1-\xi_l^2) \tag{29}$$

In the model, $\Psi = 0.5$ and ξ_l is defined by

$$\xi_l = \frac{\Phi_{dep,l}}{\Phi_{dep,l} + \Phi_{dep,s}} \tag{30}$$

The solid height h_s is evaluated after having subtracted the solid erosion loss given by eq. 25. The algorithm coupling erosion and porosity models is described in [39].

D. Computation sequence

In the present paper, the three solvers are used in a sequential manner, namely first CHARME, then SPARTE and finally FILM, without feedback impact from a solver to the previous one. This means that there is no computed impact of particle trajectories on the gas flowfield, nor impact of ice layer on the aerodynamic flowfield and particle trajectories.

Computations are run on Intel Xeon 2.4 GHz cores. The number of cores can easily be changed from one run to another. In particular, since computations with SPARTE are not parallelized according to Lagrangian trajectories but to mesh splitting, using a large number of cores is not as efficient as with Eulerian CHARME solver. CPU and memory costs are given in Table 1.

Table 1 CPU and memory costs

Solver	Number of cores	CPU cost (h)	Memory (Go)
CHARME	112	50	22
SPARTE	56	20	70
FILM	48	2	11

V. Mesh

The computational domain is shown on Fig. 2. It consists of five sub-domains, each covering one blade-to-blade passage: rotor, stator, OGV, instrumentation vane, test article, see also Fig. 1. P1 to P4 refer to row interfaces, treated with mixing plane boundary conditions.

Note that as a result of the blade generation software, the spinner generatrix is facetted. On the contrary, the manufactured spinner is continuous. The gap should stay below 0.4 mm/2% in radius.

The rotor tip gap is not modeled so that the rotor blade extends up to the shroud. Tip gap is expected to be relatively small. At room temperature, the gap was measured as 80 µm, however under cold ambient temperatures of the icing

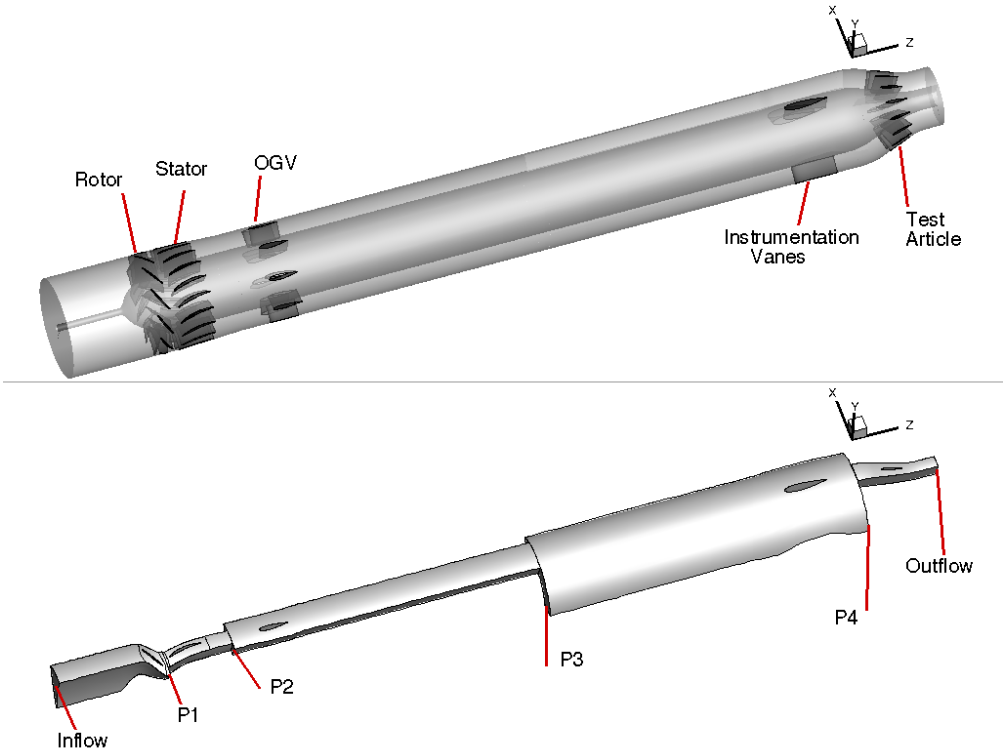

Fig. 2 Computational domain.

experiments the outer casing shrinks and the rotors just rub an abradable liner inside the outer casing. At the rig inlet, the mesh does not extend to the rotation axis but is rather limited to 5 mm in radius.

The mesh has been generated using the AutoGrid™ software. It contains 740,000 hexahedral cells in total. The first height at the walls is of 0.5 mm, leading to y^+ in the range 5-30. A wall law is applied to determine the wall friction according to the y^+ value.

VI. Simulation set-up

A. Test points

First, ice crystal trajectories and the associated fragmentation dynamics within the compressor stage are investigated for different rotor speeds. Cold conditions are considered, i.e. with a sufficiently negative wet bulb temperature to ensure fully glaciated conditions. The inlet static temperature is then −20 °C, and the rotor speed ranges from 15 000 to 33 000 RPM, see Table 2. The rig centerline TWC at 50 m s^{-1} is equal to 5.0 g m^{-3}. It is increased at higher velocities according to the inlet TWC at 50 and 75 m s^{-1} provided in [7].

Second, melting of the ice particles travelling through the test rig and ice accretion in the test article are investigated considering several operating points with wet bulb temperatures increasing from negative to positive values, thus exhibiting negligible up to significant melting levels. The points are referred to as Scan #130.02, 132.01, 131.01, and

Table 2 Rig inlet boundary conditions for the numerical simulations of ice crystal fragmentation without melting, as taken from [8]

Rotor Speed kRPM	Pstat kPa	Tunnel speed $m\,s^{-1}$	Tstat °C	Rig centerline TWC $g\,m^{-3}$
15	34	50	-20	5.0
25	34	50	-20	5.0
33	34	65	-20	6.1

131.11 in the following. Scans #130.02, 132.01, and 131.01 refer to experimental conditions reported in [7], whereas Scan #131.11 defines a fictitious operating point with conditions lying beyond Scan #131.01. This fictitious operating point is used to further characterize the sensitivity of the present numerical simulation to air inlet temperature variations and to meet the experimental observations. Rotational speed, pressure, and mass flows are constant among all operating points, while the total inlet temperature varies from -8 °C to 1 °C. The freestream centerline TWC amounts to $3.4\,g\,m^{-3}$.

The three chosen experimental test points result in accretion at various levels of severity. No accretion is observed for Scan #130.02: air temperature is too low for particles to melt. Accretion with a severity score of 3, following the nomenclature proposed by Neuteboom *et al.* [7], is registered for Scan #132.01. This case corresponds to moderate melting of particles with an average melt ratio of 12.2%. This low melt ratio produces a thin film on wall surfaces and gives the ice particles a strong sticking efficiency creating a continuous accretion growth. At the same time, experiments show that increasing particle melting ratio above 20% weakens the ice layer [34]. Therefore, for the large melting ratio of 42.2% measured for Scan #131.01 minimal accretion of the severity level of 0.5 was observed: steady build and shed, small localized accretions on leading edge-casing junction.

The operating conditions are summarized in Table 3. Except for the ranges of relative humidity (RH) measured in the tunnel, which were provided to the authors upon direct request, all input parameters used in the numerical simulations of Scans #130.02, #132.01 and #131.01 correspond to experimental characterizations reported in [7]. Neuteboom *et al.* [7] previously published RH values measured at the test article inlet, but these data are unreliable since they lead to unlikely RH levels over 100% at rig's inlet. Wet bulb temperatures were also reported, but since they strongly depend on RH, they are deliberately omitted in the present paper. Finally, only the air inlet temperature is modified for the fictitious operating point (Scan #131.11).

B. Boundary conditions

1. Gas

At the rig inlet, total pressure and temperature are specified as measured or calculated from static pressure, temperature and velocity. Dry air is considered to investigate ice crystal fragmentation at low temperature, while humid air is considered to investigate melting and accretion. The water vapor fraction is deduced according to RH

Table 3 Rig and test article inlet conditions [7] for the numerical simulations involving both fragmentation and melting. In addition to the three experimental operating points, one fictitious operating point (italic) is defined for sensitivity analysis of the melting process.

	Tunnel	Rig inlet				Rotor	Test article inlet				
	RH	P0	Massflow	T0	TWC	Speed	Melt	Severity	T0 dry	P0	Pstat
Scan #	%	kPa	$kg\,s^{-1}$	°C	$g\,m^{-3}$	RPM	ratio		°C	kPa	kPa
130.02	76-83	34.89	0.308	-8.1	3.4	26290	0.000	0.0	2.04	38.52	36.46
132.01	81-90	34.90	0.300	-3.8	3.4	26300	0.122	3.0	5.41	38.24	36.42
131.01	95-98	34.88	0.300	-0.9	3.4	26300	0.422	0.5	7.51	38.41	36.30
131.11	*98*	*34.90*	*0.300*	*1*	*3.4*	*26300*					

values measured in the tunnel flow. The RH variations between tunnel and rig inlet due to section restrictions may be considered negligible compared to the variations observed in the tunnel during the experiments. Indeed, the discrepancy has been quantified less than 8% difference on Specific Humidity which makes insignificant effect on calculated wet bulb temperature at the accretion zone. The RH at the rig inlet are respectively 83%, 90%, 97% and 98% for Scans #130.02, #132.01, #131.01 and #131.11 respectively.

The outlet massflow rate is set either as measured in the experiments or calculated from the inlet velocity and thermal conditions. Radial equilibrium is prescribed at the outlet to correctly reproduce the radial pressure distribution induced by centrifugal effects.

In the experiment, only the extended duct is insulated. On the contrary, all walls are assumed adiabatic in the numerical simulations. A no-slip condition is applied on all walls except the rotor shroud since the gap at the blade tip is not modeled.

2. Particles

Solid ice crystals are injected at the rig inlet. The experimental particle size distribution measured at 25000 RPM and −20 °C [7] is approximated by a log-normal mass distribution with a mean and standard deviation of respectively 92.2 µm and 0.48. Note that particle mass and volume distribution may be considered equivalent in the absence of melting as ice density does not vary significantly with temperature. A comparison between experimental and numerical particle mass size histograms and cumulated mass distribution is shown in Figure 3. The same size mass distribution is then used in all computations.

Neuteboom *et al.* [7] reported a non-uniform TWC over the tunnel section. A pronounced peak is observed, aligned with the tunnel centerline and the rig's rotational axis. The outer concentration is only one-third of the center value. The SPARTE solver does not presently allow setting a concentration profile depending on the radial position. In an attempt to reproduce the radial concentration profile, the inlet section is subdivided into three rings with following radial ranges: [5 mm,15 mm], [15 mm,45 mm], [45 mm,72.5 mm]. Figure 4 compares the injected relative TWC profiles

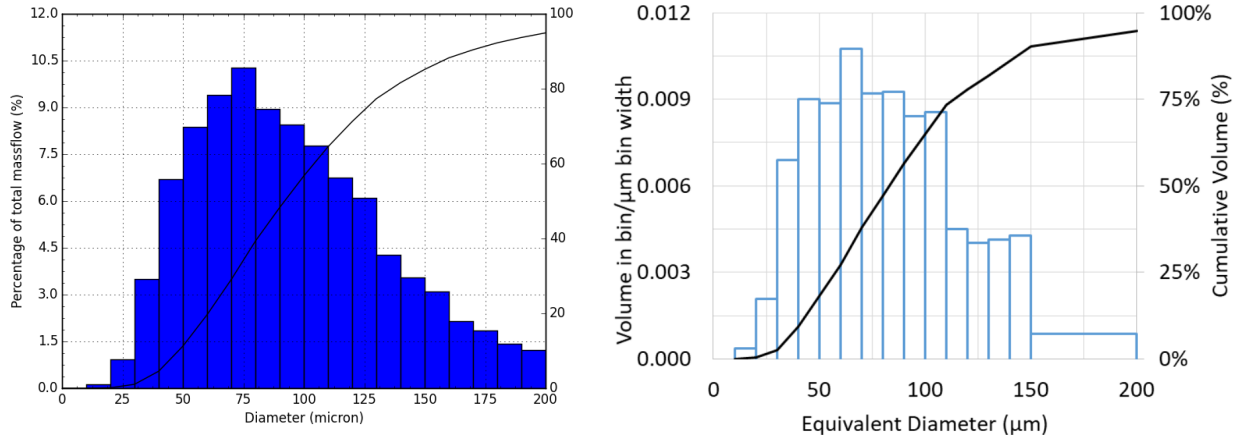

a) b)

Fig. 3 Particle size histograms at inlet to the rig, 25 kRPM, −20 °C**: a) in the computation b) in the experiment [7].**

with experimental data [7]. The same relative concentration distribution is used in all computations. The freestream centerline TWC, corresponding to the peak value, is adapted for each case.

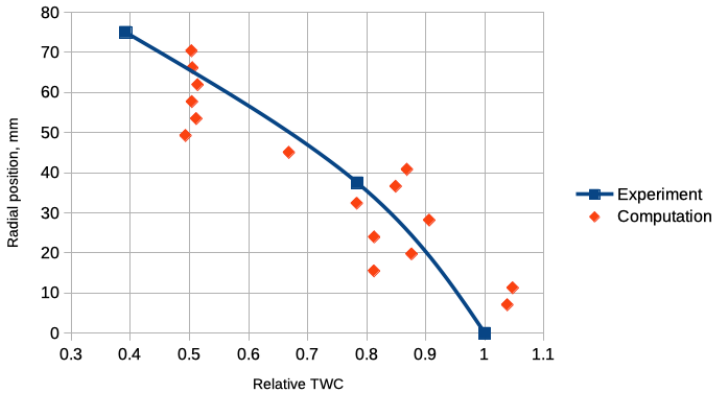

Fig. 4 Rig inlet relative TWC profile, 50 m s^{-1}**,** 25 kRPM**.**

The sphericity of injected particles is set to $\phi = 0.58$. It corresponds to highly elongated crystals, with an aspect ratio around 0.2 [40]. It is probably much less than the mean of particle clouds, for which an aspect ratio of 0.6 and a corresponding sphericity of about $\phi = 0.9$ shall be more suitable [8]. However, a sphericity of 1 has also been tested and it was found not to significantly affect the results, especially regarding the particle size downstream the rotor and the melting. Indeed, it only slightly modifies the trajectories up to the first impact since the sphericity of the fragments is drawn from a uniform distribution, as explained in section IV.B.4.

Particles are injected with a number density of about 10 mm^{-2}. At each mixing plane, particles are reinjected downstream with the same density of 10 mm^{-2}. Nevertheless, upstream the test article, particles are injected with a

number density of about $200\,\mathrm{mm}^{-2}$. These densities must be large enough to ensure satisfactory convergence on the quantities of interest, namely melting ratio and size distributions at various positions within the test rig. They also ensure to obtain a smooth distribution of mass flux deposit on walls at the level of the test article. It was verified that a multiplication of the injected particle density by a factor of 3 had no significant influence on the results.

3. Accretion

Computation of accretion is limited to the test article vane and casing. The FILM solver takes all its input from the previous solvers. No specific boundary condition is required. Note that a liquid film reaching the trailing edge does not lead to the re-injection of particles.

VII. Results for fragmentation

Figure 5 shows the evolution of the particle diameters Dv50 and Dv90 with rotor speed. Here Dvxx corresponds to the diameter delimiting xx% of the fragment volume distribution. Thus, Dv50 corresponds to the median of the fragment volume distribution. Data are extracted at the stage exit. Values plotted at 0 RPM correspond to the size distributions injected at the rig inlet; note that the log-normal distribution used in the injection plane slightly under-estimates Dv90 and over-estimates Dv10.

Both HAIC and MUSIC-haic impingement models successfully reproduce the decreasing particle size with increasing rotor speed and provide the correct orders of magnitude. The MUSIC-haic model predicts slightly larger sizes than the HAIC model, but the differences between both appear negligible. Both models overestimate the Dv50 at 15 kRPM as well as at 25 kRPM, although to a lesser extent. At 33 kRPM, a very close agreement with experiments is observed for both models. The Dv90 follows a very similar trend as it is also over-estimated at 15 kRPM, slightly under-estimated at 25 kRPM, and correctly captured at 33 kRPM. Overall, the level of agreement with experiments appears very satisfactory for both models, especially at 25 kRPM and 33 kRPM.

Figure 6 compares values of Dv10, Dv50 and Dv90 obtained with the MUSIC-haic model at the exit of stage 1 with values upstream of the stator. At 15 kRPM, similar reductions of the Dv50 are observed from the rig inlet to the stator and from the stator to the stage exit. Thus, particle impingement on the spinner/rotor and on the stator/OGV walls almost equally contributes to the size reduction at this rotational speed. On the contrary, most of the ice particle size reduction is caused by impacts on the spinner and rotor at higher rotational speeds. The Dv50 reduction between stator and OGV is roughly constant and amounts to approximately 10 µm. Similar trends may be noticed for Dv10 and Dv90.

The largest impact velocities reported in ice particle experimental database [25] are $80\,\mathrm{m\,s}^{-1}$ while the latter reach up to $270\,\mathrm{m\,s}^{-1}$ and $170\,\mathrm{m\,s}^{-1}$ on average at 33 kRPM. Thus, both models seem to correctly extrapolate to impact velocities which are representative of realistic engines. This behavior could be because hailstone experimental impact data with significantly larger impact velocities (up to $200\,\mathrm{m\,s}^{-1}$) were also included to calibrate the parameters of these models [25].

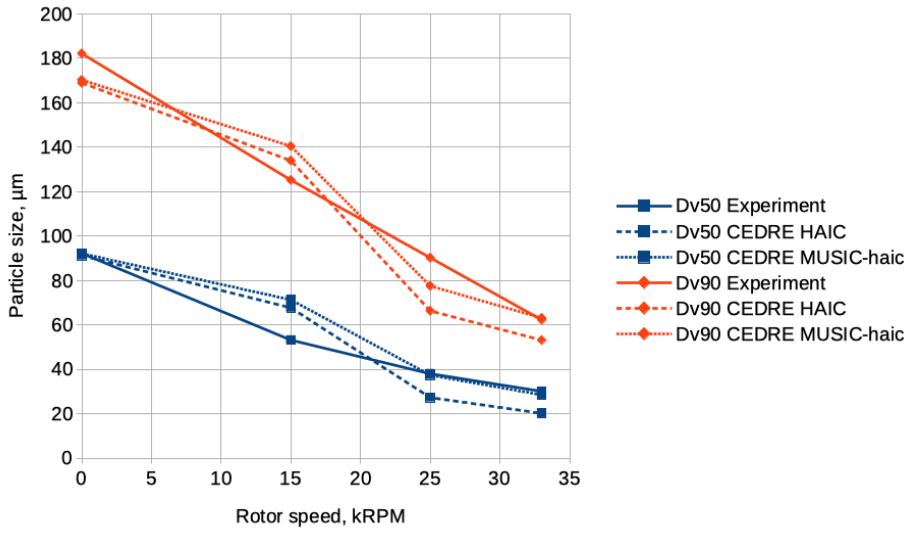

Fig. 5 Particle size with respect to rotor speed, comparison between state-of-art model (HAIC), new model (MUSIC-haic) and experiments at the exit of stage 1. Note that the values reported for vanishing rotor speed correspond to numerical and experimental inlet values.

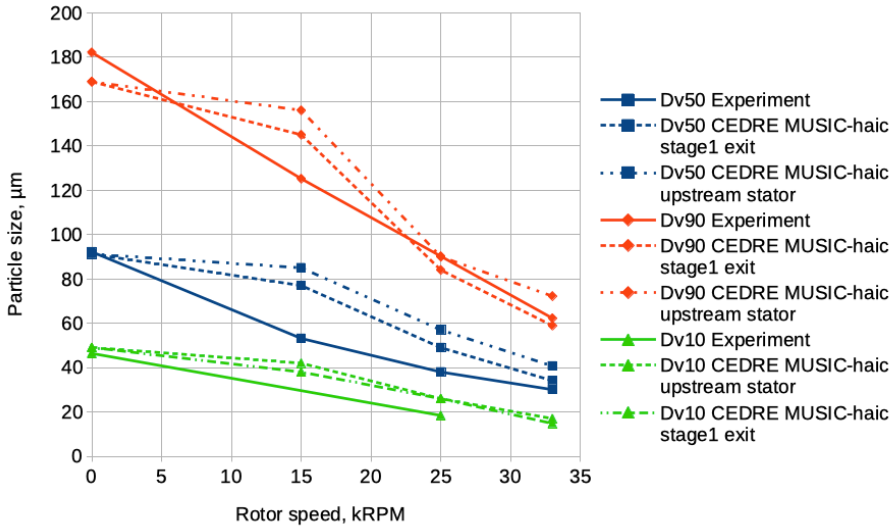

Fig. 6 Particle size with respect to rotor speed and location. For the numerical simulations, the Dv10, Dv50 and Dv90 obtained downstream the rotor and the exit of stage 1 with the 'MUSIC-haic' model are shown and compared to the experimental values at the exit of stage 1.

The particle size histogram at the exit of stage 1 is plotted for both simulation and experiments in Figure 7. A good agreement is observed despite a slight shift towards larger diameters of the numerical volume and cumulated volume distributions compared to experiments. These results indicate that the numerical averages performed on the mixing plane separating rotor and stator do not significantly deteriorate the downstream size distribution. However, a reasonable

assumption on the upstream particle size distribution must be made, and its parameters must be computed for each mixing plane ring. As for the rig inlet, the ice crystal particle distributions are assumed to follow a log-normal mass distribution on each mixing plane ring.

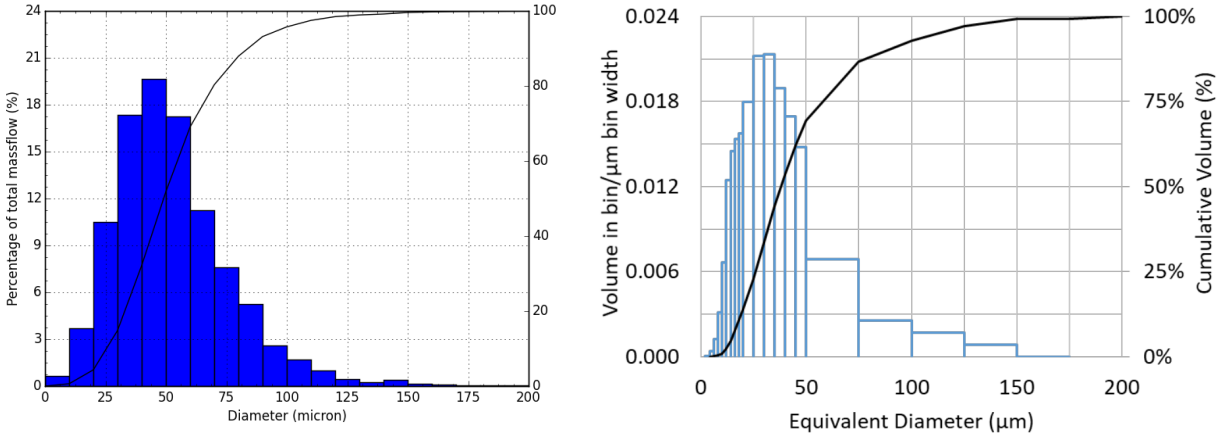

a) b)

Fig. 7 Particle size histograms at stage 1 exit, 25 kRPM**,** −20 °C**: a) in the computation b) in the experiment [7].**

Figure 8 shows how the radial relative TWC profile evolves with the axial position in the test rig for the case 25 kRPM. The relative TWC is calculated as the local TWC divided by the freestream centerline TWC. To help understand TWC profiles, particle trajectories are pictured in Fig. 9 in the meridian (z,r) frame and colored by the particle size. Just upstream of the rotor, the relative TWC has increased over 1 at a low span due to the rotor spinner. Two peaks are visible at two different radial positions, corresponding to the two curvatures of the fore spinner. Considering that the spinner is slightly facetted in our model contrary to continuous reality, and also that the inlet TWC profile is constant over rings (Fig. 4), the two angle concentration may not have happened in the actual rig but instead a smooth concentration growth towards low radius. TWC at low span continues increasing past the rotor, up to 2. At larger radii, the concentration stays similar downstream and upstream of the rotor. However, at the stator exit, the concentration is drastically reduced over a large portion of the span, and particles concentrate in the upper part. This is caused by particle impingement on the spinner and particle centrifugation by the rotor, as illustrated by particle trajectories pictured in Fig. 9 a) or by radial particles velocities at the interface between rotor and stator (Fig. 10). Impacts on the rotor blade are clearly visible by trajectories pointing out upwards along the trajectories against the airflow.

The stator casing is not at a constant radius but decreases by 3.5 mm over a distance of 94 mm, corresponding to a 2.2° converging conical shape. Most of the particles impinge the casing on this conical portion and bounce off with a negative radial velocity. Thus, trajectories become centripetal due to bouncing, as shown in Fig. 9 b) close to the casing, upstream of the OGV. The discontinuity in the plot of trajectories corresponds to the mixing plane delimiting

the stator/OGV interface on this subfigure. Be also aware that the density of plotted trajectories at a certain radius downstream the mixing plane has no meaning regarding the statistical probability; indeed the transported particle mass flow may be very low. Centrifugal trajectories are still visible upstream of the interface but disappear downstream up to impacts on the OGV vane as shown in Fig. 9 c). This is due to the numerical treatment at the mixing plane: particles are re-injected downstream with the average velocity vector computed from upstream incoming particles. When centripetal and centrifugal trajectories of particles merge, the resulting average velocity is mainly axial. This behavior illustrates the well-known issue of crossing trajectories, which occurs when treating a dispersed phase with standard Eulerian methods [41]. Separate mixing-plane averages based on a distinction between the sign of the radial velocity component could be defined to circumvent this issue.

Particles re-injected downstream the stator/OGV mixing plane in the annulus' outer portion are isolated in Fig. 9 d). Since they follow centripetal trajectories, they contribute to the spatial redistribution of the particles over the annulus and thus repopulate the inner part of the span. As a consequence, TWC increases in the radius range between [50-65 mm] downstream the OGV compared to the stator exit, as shown in Fig. 8 b) with respect to a). Simulations using the MUSIC-haic model predict three peaks, respectively, at 55 mm, 60 mm and 65 mm radii, whereas those using the HAIC model give a smoother profile around radius 55 mm but similar at the larger radial position (remember the presence of several peaks is attributed to the facetted spinner geometry). However, both models give a similar profile downstream of the rotor (Fig. 8 a). The predicted level of relative TWC is compared to experimental data at the exit of first stage (Fig. 8 b). These data were previously unpublished, although dimensionless profiles are available in [7]. Whatever the model, the predicted TWC is up to five times lower than the measurement at one-third span, for an experimental uncertainty of $\mp 20\%$. The correct order of magnitude is found at two-third span. No experimental data is currently published at the outermost portion of the annulus. However efforts to measure, during recent test campaigns, the water concentration close to the casing did not highlight any evidence of massive concentration. On a contrary, a drop off of TWC was observed rather than a spike. It is also confirmed while estimating the TWC at the casing through particle mass flow concentration in the system. Conservation indeed applies since the temperature is low enough below 0 °C to limit losses through sublimation or wall deposition.

Looking at the profiles downstream, the radial position of TWC peaks located at radius 60 mm and over is conserved from stage 1 exit to the middle of the extender duct (Fig. 8 c). This probably results from the mostly axial particle injection velocity at the stator/OGV interface. On the contrary, the peak below 60 mm radius is shifted towards the hub, indicating that the centripetal effect induced by particle impacts on the conical casing is still present. At the inlet to the test article (Fig. 8 d), there is still a peak close to hub, while the peak at two-third span is shifted and merged with the high concentration at casing. The mid-span region is depopulated, contrary to (previously unpublished) measurement. Again, a massive concentration at the casing has not been measured. The origin of this discrepancy is still unknown. Note that gravity effects that were not taken into account in the present computations are suspected to have an influence

on the particle trajectories but this point will need to be further investigated in future work.

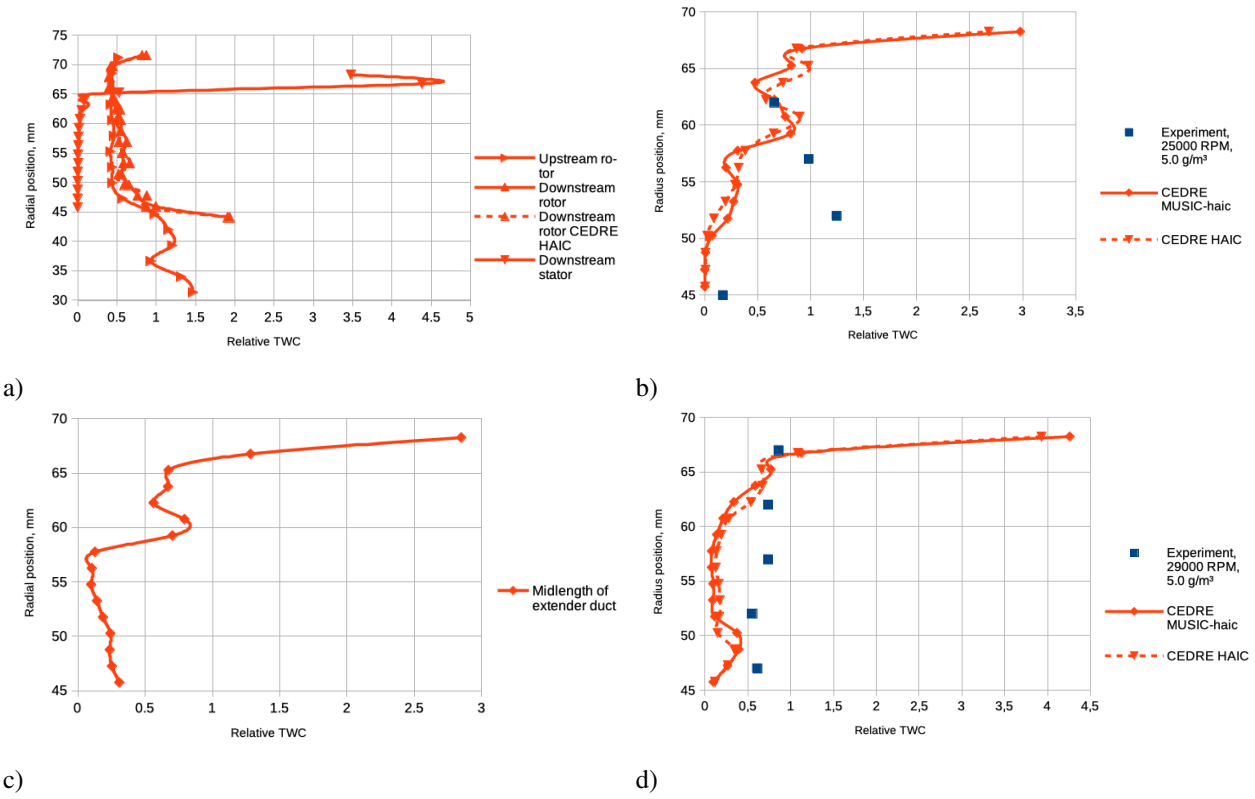

Fig. 8 Radial relative TWC profiles, 25 kRPM**, MUSIC-haic model unless specified: a) in rotor and stator, b) at stage exit, c) at mid-length of the extender duct, d) at the inlet to the test article.**

TWC profiles are also plotted for the two other rotor speeds in Fig. 11, while corresponding particle trajectories can be seen in Fig. 12. At lower rotor speed, the effect of centrifugation appears reduced. Then, a large number of particles impinge on the conical part of the casing. At the stator/OGV interface, centripetal and centrifugal beams are still disjoint. Consequently, the particles injected on the downstream side of the mixing plane still exhibit centripetal and centrifugal directions according to their radial position, the former being limited to the most outer portion of the annulus. The two beams cross just downstream, in front of the OGV vane. They are plotted isolated from each other in the OGV and the extender duct. The increase in TWC at a low span is then lower than at 25 kRPM. After bouncing on the casing, particles are redirected towards the hub and merge with the particles following the stator casing slope. The merging of the two trajectory beams produces a peak in the radial range [60-65 mm]. The latter is progressively shifted towards the hub within the extender duct.

At 33 kRPM, TWC profile and particle trajectories look similar to the ones at 25 kRPM.

Finally, the average particle velocity measured at instrument vane inlet at 25 kRPM amounts to 82 m s^{-1} in the experiments and 86 m s^{-1} in the numerical simulations.

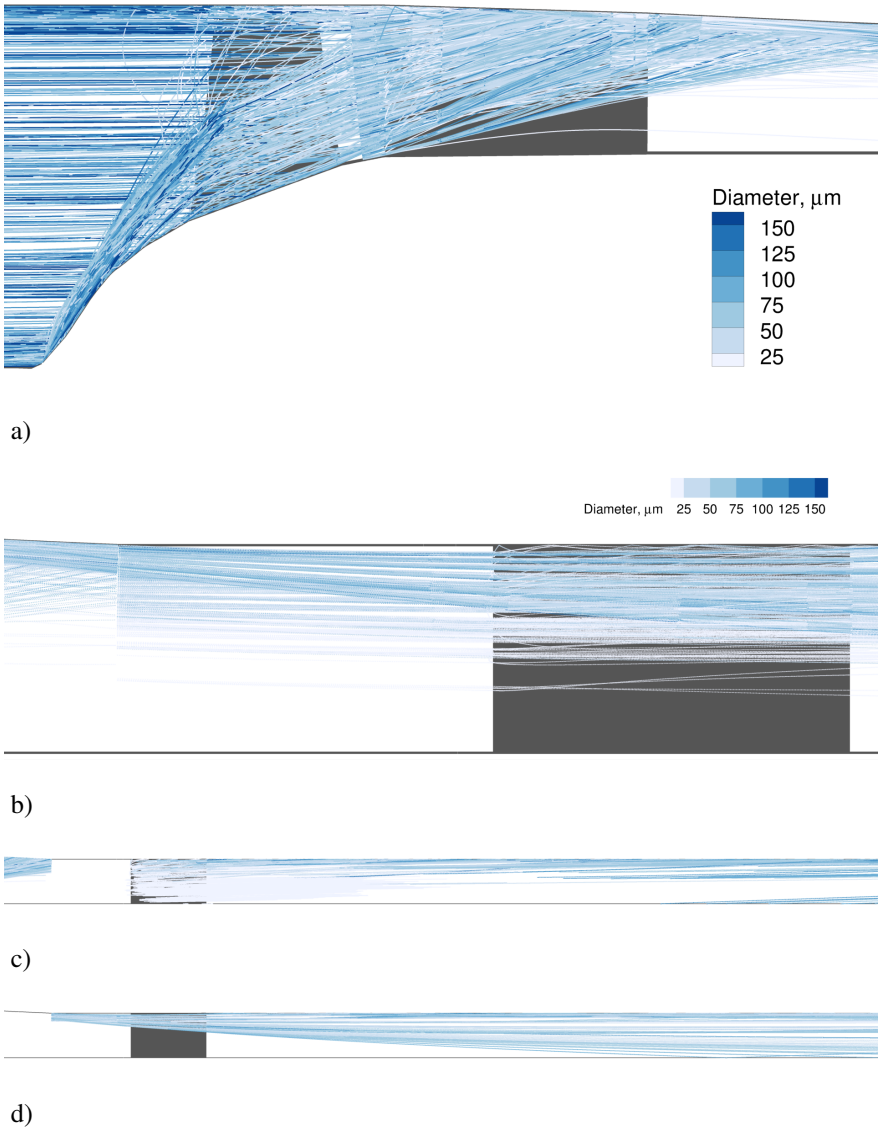

Fig. 9 Trajectories of particles, 25 kRPM**, a) near rotor and stator, b) near OGV, c) limited to centripetal trajectories, d) limited to the outer portion of the annulus in the mixing plane.**

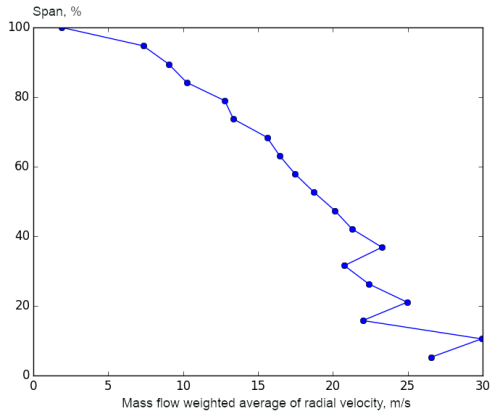

Fig. 10 Radial distribution of particles radial velocity in the plane between rotor and stator, 25 kRPM**.**

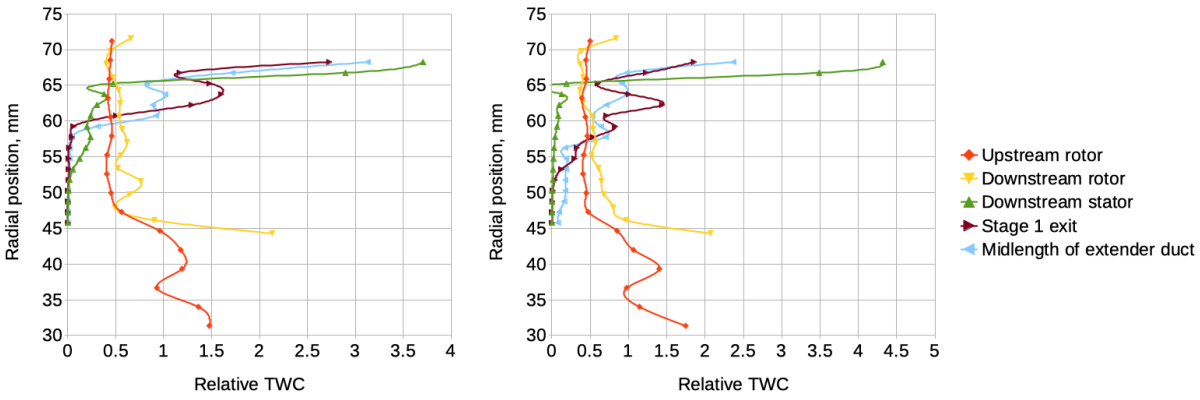

Fig. 11 Radial relative TWC profiles at different locations, 'MUSIC-haic' model, 15 kRPM **(left)** 33 kRPM **(right).**

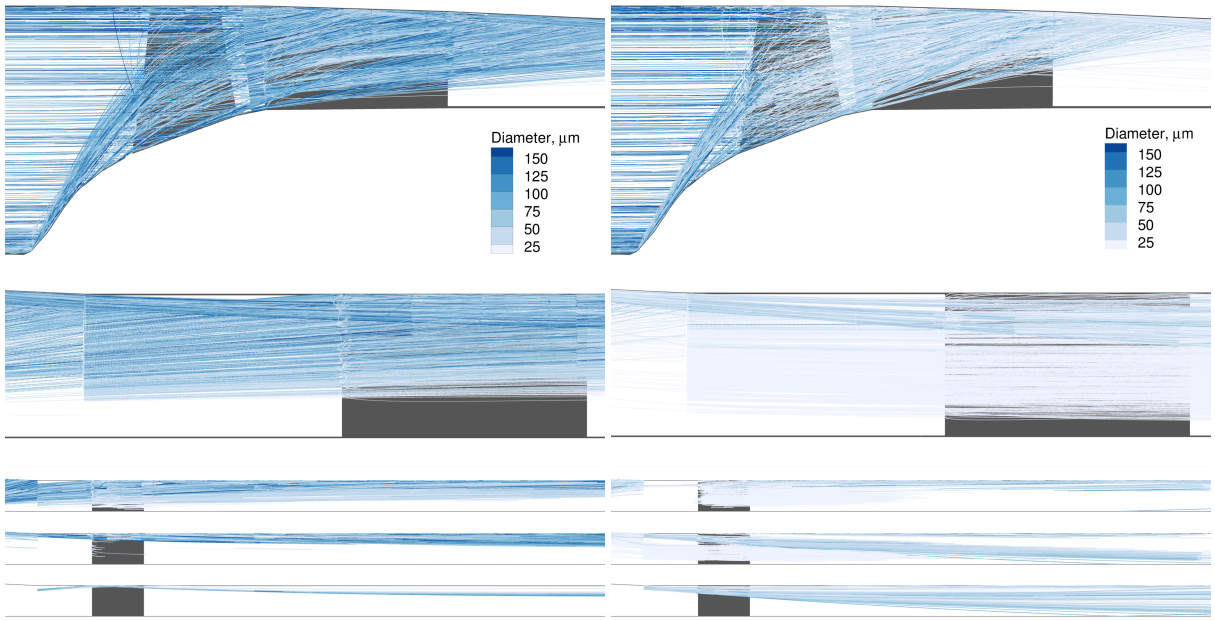

Fig. 12 Trajectories of particles, ***left)*** 15 kRPM, ***right)*** 33 kRPM, ***top)*** **near rotor and stator,** ***middle top)*** **near OGV,** ***middle)*** **limited to centrifugal trajectories,** ***middle bottom)*** **limited to centripetal trajectories,** ***bottom)*** **some isolated trajectories.**

Table 4 Numerical and experimental [7] gas flow parameters in the instrumentation vane.

Scan #	130.02		132.01		131.01	
Parameters	CEDRE	*Experiment*	CEDRE	*Experiment*	CEDRE	*Experiment*
P0, kPa	37.64	*38.52*	37.59	*38.24*	37.48	*38.41*
Pstat, kPa	35.91	*36.46*	35.97	*36.42*	35.80	*36.30*
T0, °C	2.5	*2.0*	6.8	*5.4*	9.5	*7.5*

VIII. Results for melting

A. Gas flow field

To validate the quality of the numerical gas flow field, numerical and experimental data are compared in the instrumentation vane in Table 4. All data are extracted at the experimental probe locations. The total and static pressures are under-estimated by approximately 0.9 kPa and 0.5 kPa, respectively. Either the rotor performance is under-estimated, with a pressure ratio of 1.08 instead of 1.10, or losses in the duct are over-estimated. On the contrary, the total temperature is over-estimated, and the discrepancy increases with the inlet temperature. The difference amounts to 0.5 °C for Scan #130.02, 1.4 °C for Scan #132.01 and 2.0 °C for Scan #131.01. Here again, either the efficiency factor is under-estimated, or thermal losses in the duct are under-estimated. Discussions with the experiments'team indicate that temperature drops from 1 to 3 °C were measured between inlet and exit of the extender duct during dry tests, *i.e.* in the absence of ice particles. Thermal losses may occur at the hub or by conduction in the insulated casing to upstream and downstream parts. No such effects may be presently captured in the numerical simulations as all walls are assumed adiabatic. However, it should be noted that, while including in the modelling the nacelle lip and the rotor tip gap and using a much finer mesh (30 million elements, 40 times more than in our case), Nilamdeen *et al.* [12] reported very low discrepancies between computed and measured temperatures (0.4% at most, 0.14% in average corresponding 0.4 °C).

Table 5 provides numerical flow parameters at the test article inlet. RH is comprised between 45% and 57%. Following the analysis by [34], melting is expected to occur when the wet bulb temperature Twb based on static temperature is positive. Twb increases from largely (−5.8 °C) to slightly (−1.7 °C) negative values from Scan #130.02 to Scan 132.01. Consequently, no melting is expected in the numerical simulation of those points, contrary to experiments where melting occurs in Scan #132.01. It then reaches positive values of respectively 1.2 °C and 3.0 °C for Scans #131.01 and #131.11, for which melting is expected to be numerically predicted. Accretion is susceptible to occur when the wet bulb temperature Twb0 calculated with the total temperature is positive. One can see that it is negative uniquely for Scan #130.02, indicating that ice accretion may occur from Scan #132.01.

B. Melting

The ice particles' melt ratio was measured at the inlet to the test article. It is important to remember that melt ratio measurement is not exact but should be considered more as a scale. Indeed, the ratio of LWC to TWC from the SEA

Table 5 Gas flow parameters at the test article inlet as computed by CEDRE.

Scan #	130.02	132.01	131.01	131.11
Pstat, kPa	35.92	35.90	35.79	35.82
Tstat, °C	-0.5	3.8	6.5	8.5
RH, %	45.7	50.6	55.9	56.6
Twb, °C	-5.8	-1.7	1.2	3.0
Twb0, °C	-3.5	0.5	3.7	5.6

Table 6 Melt ratio and temperatures, MUSIC-haic model.

		Melt ratio at test article inlet, %	
Scan #	Inlet T0, °C	CEDRE	*Experiment*
130.02	-8.1	0.0	*0.0*
132.01	-3.8	0.0	*12.2*
131.01	-0.9	22.2	*42.2*
131.11	1.0	41.2	

multi-wire probe was used to measure this parameter. However, neither the TWC nor LWC from the SEA multi-wire probe are measured very accurately. LWC can be as much as 10% low, and TWC can be off by a factor of 2-4. LWC may also display a false response caused by ice crystals, but the melt ratio has been corrected to take that into account.

Table 6 compares measurements and computations performed with the MUSIC-haic impingement model. As expected, according to wet bulb temperatures calculated from numerical results, melting is predicted for Scan #131.01, but not for Scan #132.01, contrary to experiments. The amount of melting for Scan #131.01 is less than measured and corresponds more to what was measured for Scan #132.01. Similarly, computed melt ratio for the fictitious point #131.11 corresponds to the measurement for Scan #131.01.

The average melt ratio appears to be very sensitive to the inlet temperature. In the experiments, the melt ratio rises from 0 to 12% within an increase by 4.3 °C of the inlet total temperature, and from 12 to 42% for an additional rise by 2.9 °C. It means that a temperature rise by 1 °C leads to roughly 10% increase in the melt ratio. This slope is correctly reproduced in the simulations since a temperature rise by 1.9 °C increases the melt ratio from 22% to 41%.

Finally, the numerical simulations predict the onset of melting at higher inlet temperatures compared to experiments. The temperature shift roughly amounts to 4 °C, 2 °C coming from the shift in the inlet total temperature and an additional 2 °C coming from the discrepancy at the test article inlet. The latter is attributed to the gas flow solver and will not be discussed further in this paper, while the former is attributed to the particle solver and is investigated in a next section.

IX. Results for accretion

The height of the ice layer computed by the solver is used to produce an illustration of ice accreted on walls. The surface mesh is deformed by moving the nodes in the direction normal to each face by a distance according to the

height of the ice layer. The resulting shapes are plotted in Fig. 13 and compared to photos taken during the experiments, extracted from Neuteboom *et al.* [7]. The figure presented here corresponds to the final accretion that was observed after 6 min. In the simulations, the computation of accretion is set according to this duration, except for the case with a severity of 3. Indeed, for the latter, experiments exhibit build and shed cycles during a rough total period of 130 s before infinite growth starts [10]. Therefore, in that case (namely the computation for Scan #131.01), the accretion duration is reduced to 230 s.

For Scan #130.02, no accretion is observed, neither in the experiment nor in computation. Indeed, in both cases, the particle temperature is too low to enable melting.

For Scan #132.01, a severity of 3 is experimentally observed. On the contrary, the computation exhibits no accretion due to the absence of melting. However, a large accretion is computed for Scan #131.01 and can be compared to severity 3 experimental observations. In the latter, ice is accreted on the vane leading edge and on the casing, both upstream and downstream of the leading edge. The ice layer extends to one-fifth of the vane passage approximately. On the casing, ice covers the full azimuthal range. In the computation, the ice layer extends on the vane leading edge and the shroud, similarly. The ice accreted on the shroud forms a 13 mm-thick bump upstream the vane, located at the inflection point. Erosion is not sufficient to limit its growth, and in reality shedding is probably the limiting factor, however shedding is not modeled. The models may also suffer from the lack of experimental data at very low impinging angle. A spike with an even larger depth (16 mm in average in span corresponding to the two-thirds of of the duct height, with a peak at 23 mm) is also produced from the shroud right in front of the vane leading edge. It compares surprisingly well with the experimental observation, although one would instinctively suppose it has grown from the vane surface rather than from the shroud. The ice layer extends downstream on the shroud, with a noticeable height along up to about 40% of the vane chord. The ice accreted on the vane is concentrated at the tip, with an extension in chord similar to the accretion on the shroud. It spreads almost from one vane to the next one, as in the experiment. On the leading edge, some ice is visible at lower span but with a very limited thickness. Since the liquid water content is higher than in the experiment, the solver indicates that accretion is computed according to glaze ice regime (see section IV.C). The authors have shown in [42] that correcting the 2 °C discrepancy in the gas temperature at the test article (through an energy sink term in the rotor passage) on one hand, and injecting crystals at the test article inlet with the measured size distribution, concentration and melt ratio on the other hand, lead for Scan #132.01 to rime icing and ice layer on the vane that compares much better with the experiment.

For Scan #131.01, a severity of 0.5 is experimentally observed. The key characteristic is continuous build and shed cycle. The end frame plotted on Figure 13 shows ice accreted on the leading edge, at the junction with the casing, to a small extent. The computation at fictitious Scan #131.11 is in agreement with this picture. However the build and shed cycle cannot be captured numerically without modelling the heat transfer between the warm metal and accreted ice. Accretion is highly dependent on the heat transfer characteristics of the metal substrate. Adiabatic wall conditions will

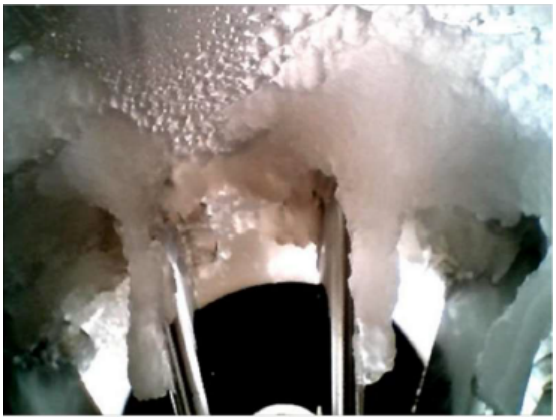

a) Experiment - Severity 3

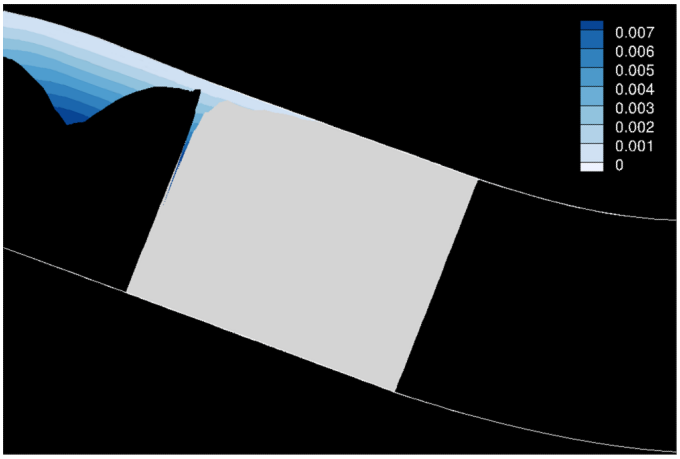

b) Computation - Scan #131.01 - Severity 3 - Ice accreted on casing, meridional view

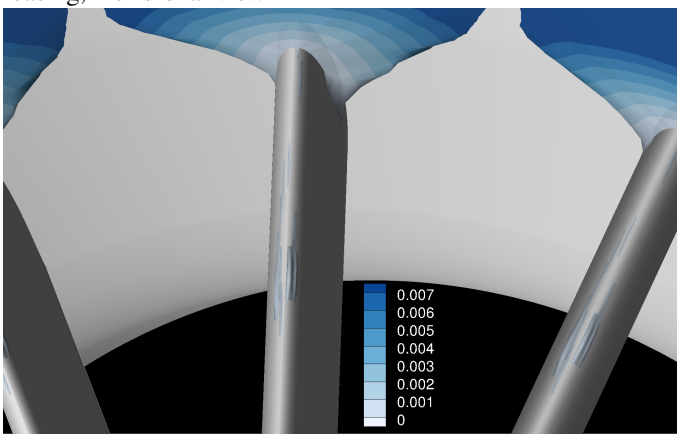

c) Computation - Scan #131.01 - Severity 3 - Ice accreted on vane

d) Experiment - Severity 0.5

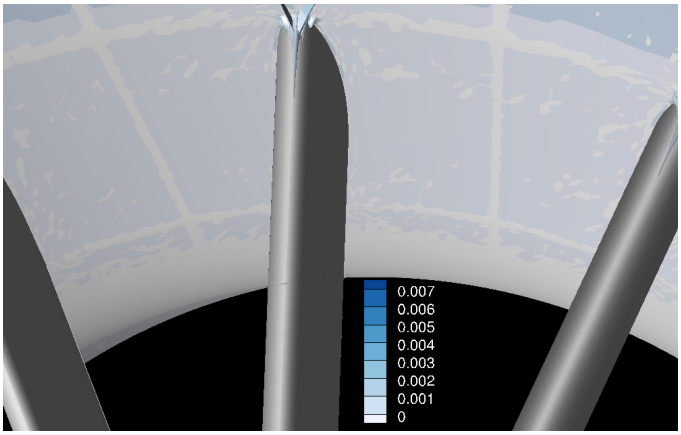

e) Computation - Scan #131.11 - Severity 0.5

Fig. 13 Accreted ice on test article vane and casing in experiment and computation (colored by the height of ice in meters).

not suffice in capturing the accurate prediction of ice accretion. Ice particles have to cool the wall to near freezing to enable accretion. At some steady state point in time, there is continued heat transfer into the walls from the heated compressor flow that balances the heat sink of the impinging ice crystals and phase change. While these heat transfers are in flux, there is continual build and shed. But once the temperature of the wall is reduced to zero and heat transfer stabilizes at some near zero value, then accretions anchor and grow. Heat transfer does not always seem to reach zero, that is because there is some low level heat transfer between the inner casing wall and outer wall.

To conclude, results show that a shift of about 2 °C in the air inlet total temperature is at this point necessary to match numerical simulation and experimental data regarding melting and accretion.

X. Further analysis of the numerical results

To better understand the previous numerical results compared to measurements, further details regarding the computed data are given and discussed below. Figure 14 plots the evolution of flow and particles parameters from inlet to outlet, as averaged in mixing planes. One can see in Figure 14b that the airflow temperature increases strongly during its passage through the rotor for all configurations. This is in accordance with the enthalpy increase due to the flow compression at the rotor level. An additional temperature rise related to kinetic energy transformation toward pressure is also observed at the stator for all Scans. Among all these scans, only Scan #130.02 shows negative temperature along the entire compressor rig. In Scans #132.01, #131.01 and #131.11, the flow temperature is far above 0 °C. The wet bulb temperature follows the same increasing slopes (Figure 14c) but it stays below 0 °C downstream the rotor for Scan #132.01. On the contrary, the total wet bulb temperature decreases in the rotor (Figure 14d) but remains positive from Scan #132.01.

Figure 14e plots the particles Mean Mass Diameter (MMD) and its Root Mean Square (RMS). It can be seen that particles fragment mainly in the rotor: the average particle diameter decreases from 100 to 40 microns. Through the stator, particle diameter decreases from 40 to 30 microns. Downstream the stator, particles diameter remains approximately constant at 28 microns, exhibiting very low fragmentation at the OGV, Instrumentation vane or Test article. It also appears that particles fragmentation is accompanied by an increase in particle sphericity. Indeed, the latter is chosen randomly in the range [0.6; 1] after wall impact, thus leading to a mean sphericity of 0.8 at the exit of the rotor (Figure 14f) while the injected particles had a sphericity of 0.58. For Scans #131.01 and #131.11, the sphericity still increases downstream the rotor due to melting.

Figures 14g and 14h plots respectively the particles temperature and melting ratio. The particle temperature is on average negative throughout the rig for Scans #130.02 and #132.01 and no melting (or almost none) is observed. However, it is not monotonously increasing: indeed, the particle temperature is slightly reduced in the OGV. This point will be further discussed later. For Scans #131.01 and #131.11, the particle temperature reaches 0 °C on average downstream of the stator. Particles start to melt in the rotor. This behavior is in accordance with the levels of wet bulb

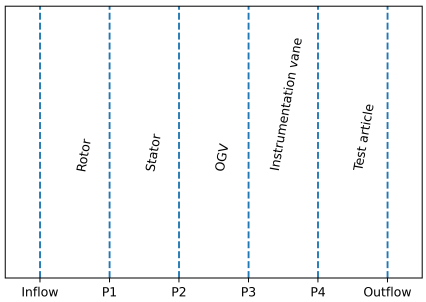
Rotor
Stator
OGV
Instrumentation vane
Test article
Inflow
P1
P2
P3
P4
Outflow

(a)

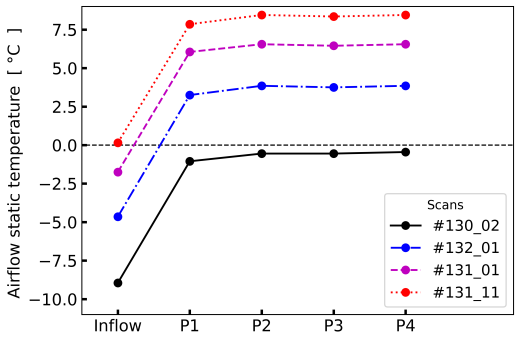
Airflow static temperature [°C]
Scans
#130_02
#132_01
#131_01
#131_11
Inflow
P1
P2
P3
P4

(b)

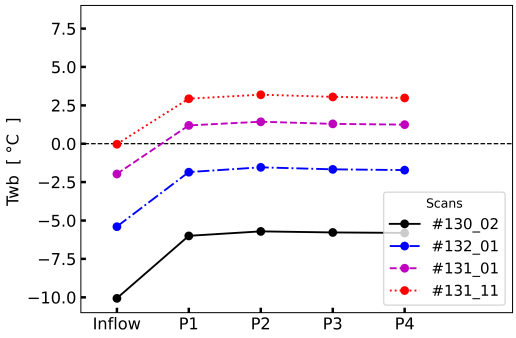
Twb [°C]
Scans
#130_02
#132_01
#131_01
#131_11
Inflow
P1
P2
P3
P4

(c)

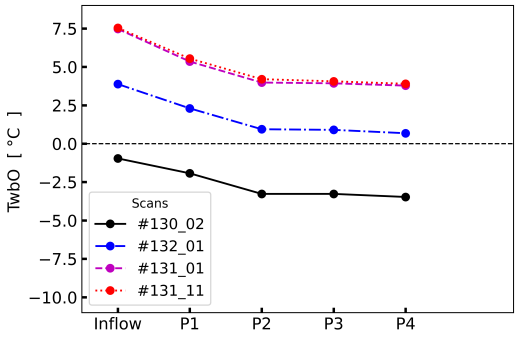
TwbO [°C]
Scans
#130_02
#132_01
#131_01
#131_11
Inflow
P1
P2
P3
P4

(d)

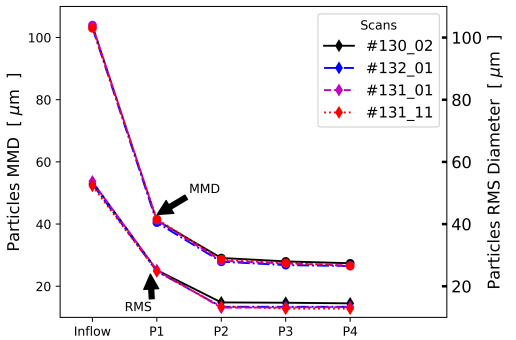
Particles MMD [μm]
Particles RMS Diameter [μm]
Scans
#130_02
#132_01
#131_01
#131_11
MMD
RMS
Inflow
P1
P2
P3
P4

(e)

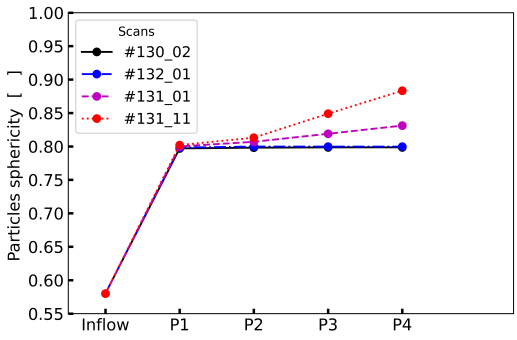
Particles sphericity [ ]
Scans
#130_02
#132_01
#131_01
#131_11
Inflow
P1
P2
P3
P4

(f)

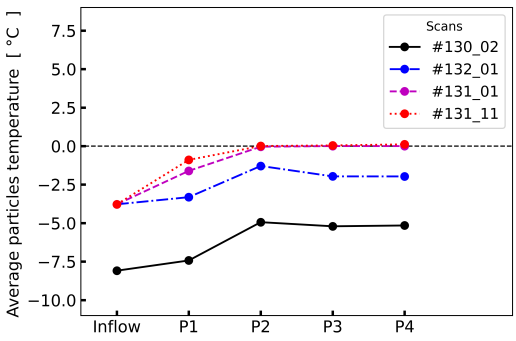
Average particles temperature [°C]
Scans
#130_02
#132_01
#131_01
#131_11
Inflow
P1
P2
P3
P4

(g)

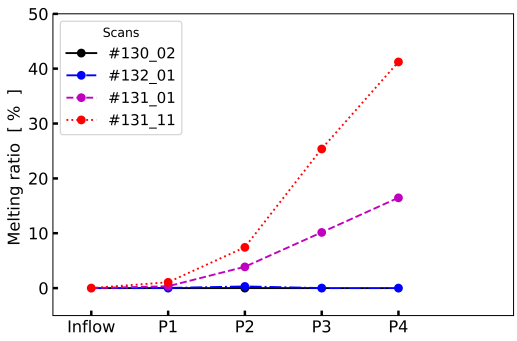
Melting ratio [%]
Scans
#130_02
#132_01
#131_01
#131_11
Inflow
P1
P2
P3
P4

(h)

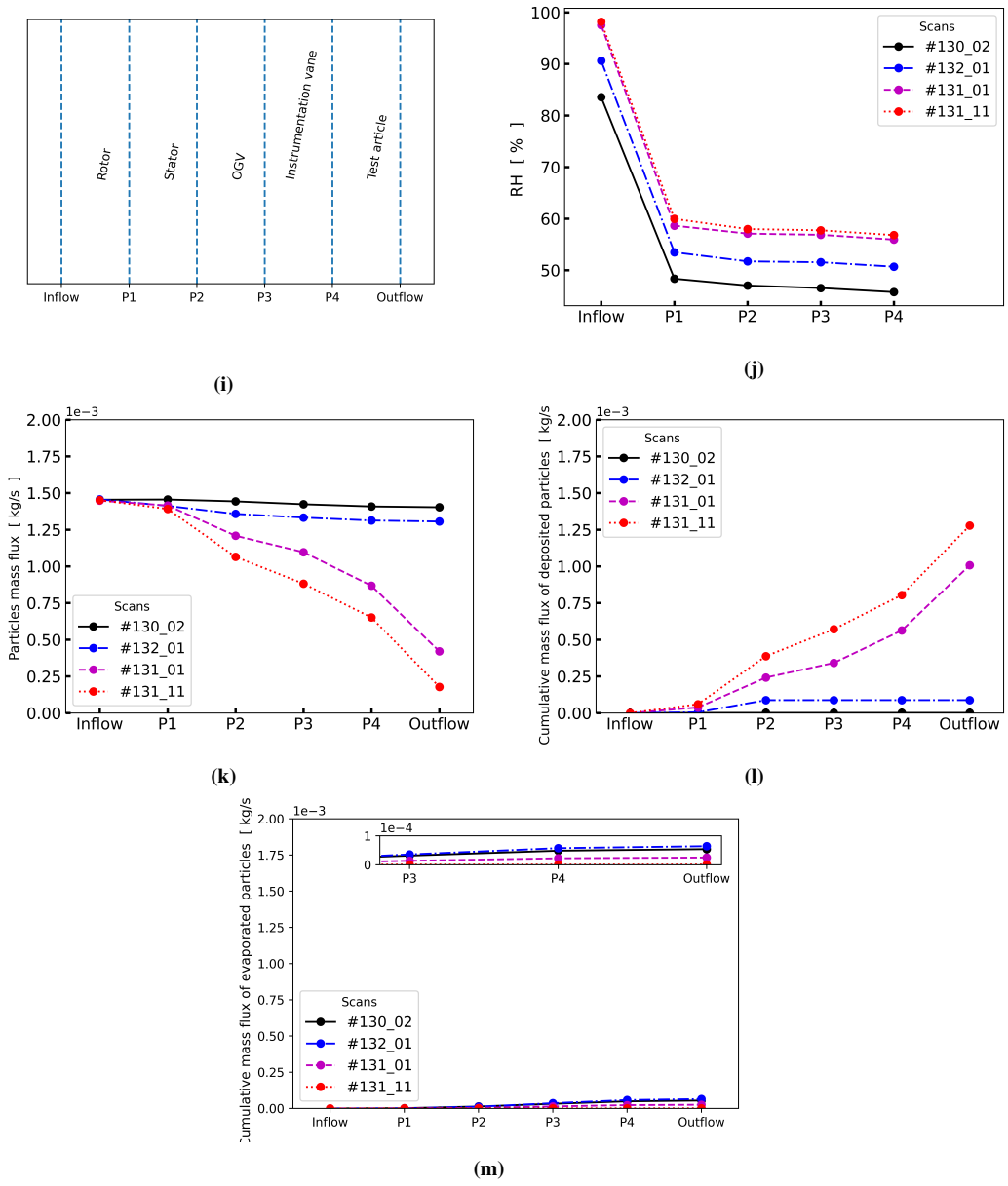

Fig. 14 Comparison of averaged flow and particle characteristics at the inlet and in mixing planes for Scans #130.02, #132.01, #131.01, #131.11, *a) and (i)* Overview of the compressor rig, *b)* Airflow static temperature, *c)* Wet bulb temperature, *d)* Wet bulb temperature calculated with total conditions, *e)* Particles MMD and RMS Diameter, *f)* Particles sphericity, *g)* Particles average temperature, *h)* Particles melting ratio, *j)* Relative Humidity, *k)* Particles mass flux at the inlet of each module, *l)* Mass flux of particles deposited on walls at each module, *m)* Mass flux of evaporated particles at each module

temperature.

The evolution of particles mass flux along the compressor rig is then plotted: the mass flux of travelling particles (Figure 14k), the mass flux of evaporated particles (Figure 14l), and the mass flux of particles deposited at walls (Figure 14m). First, it can be seen that particle mass flux through mixing planes decreases along the compressor rig for all Scans. This decrease is reinforced as the inlet temperature rises. For Scan #132.01, the decrease occurs in the rotor and stator only: the mass flux is constant downstream. The drop is almost fully compensated by deposition on walls. Since deposition is only possible for melted particles, it means that some particles are melted, even if the melting ratio is almost 0 in average (Figure 14h). A small amount of evaporation/sublimation is occuring from rotor exit to test article inlet. This point will be further discussed later. For Scans #131.01, the deposition in the test article does not fully compensate the mass flux drop downstream the instrumentation vane: indeed, evaporation occurs in the test article. On the contrary, for Scan #131.11 deposition fully compensates the mass flux drop. in For Scan #130.02, since particles are entirely solid (Figure 14h), no deposition is recorded; the mass flow drop (Figure 14k) is caused by particle sublimation.

XI. Towards an explanation for the discrepancy with respect to experiments

We now focus on Scan #132.01 in an attempt to explain the discrepancies between simulations and experiments regarding accretion. As previously mentioned, although no accretion is numerically obtained contrary to the experiment, some of the particles melt in the rotor and the stator and deposit on walls at these locations. A small amount of evaporation/sublimation is also observed downstream tof he rotor.

Figure 14g shows the average particle temperature at mixing planes along the compressor rig. For Scan #132.01, a temperature increase is observed from the mixing plane P1 to the mixing plane P2, followed by a small decrease between P2 and P3. This section aims to give more insight into this behavior. Figure 15 plots the histograms of particles melting ratio at mixing planes. These histograms show the evolution of particles melting ratio along the compressor rig. Although the wet bulb temperature shows negative values stipulating that melting does not occur for this scan, histogram plots show that a small number of particles are melted. The wet bulb temperature is based on average data, therefore, can not characterize local phenomena. At the mixing plane P1, more precisely at the exit of the rotor module (P1 left), most particles exhibit a low melting ratio. The average melting ratio is 0.8%. Nevertheless, a small amount of particles is strongly melted since they exhibit a melting ratio of up to 20%. Figure 16 shows that melted particles are at 0 °C and if their diameters can reach 50 µm, the most melted particles have really small diameters (below 5 µm). A more severe melting process is observed at the mixing plane P2, i.e., at the exit of the stator module. The average melting ratio is 1.6%, but particles with a melting ratio up to 90% are recorded. The size of melted particles is increased compared to P1. Contrary to these two first mixing planes, mixing planes P3 and P4 do not show any melting. This evolution of the average melting ratio is in accordance with Figure 14h. This result could partially explain the evolution of particles temperature observed at Figure 14g, where the temperature increases from plane P1 to P2

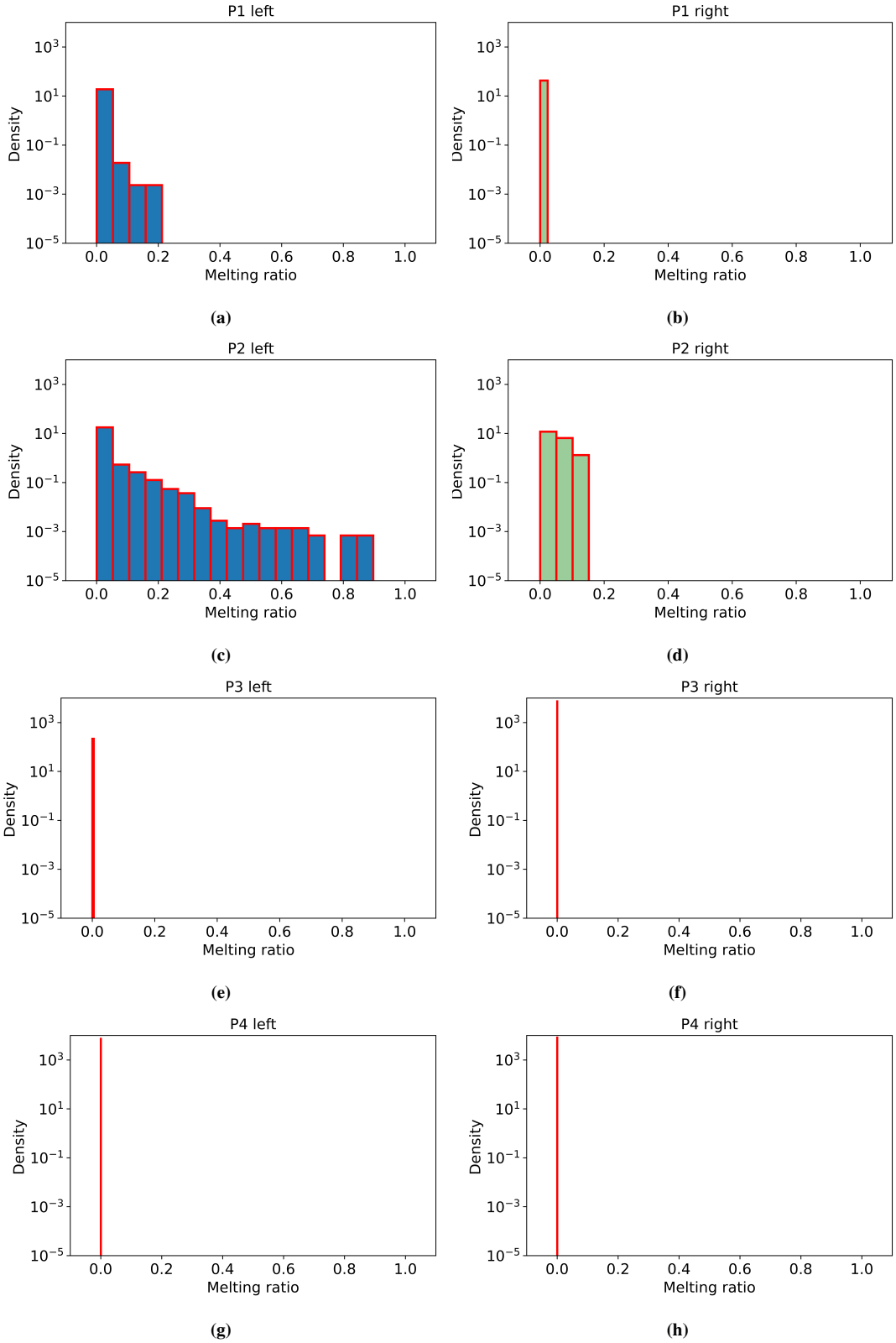

Fig. 15 Histogram of particles melting ratio on upstream (left) and downstream (right) sides of mixing planes for Scan #132.01

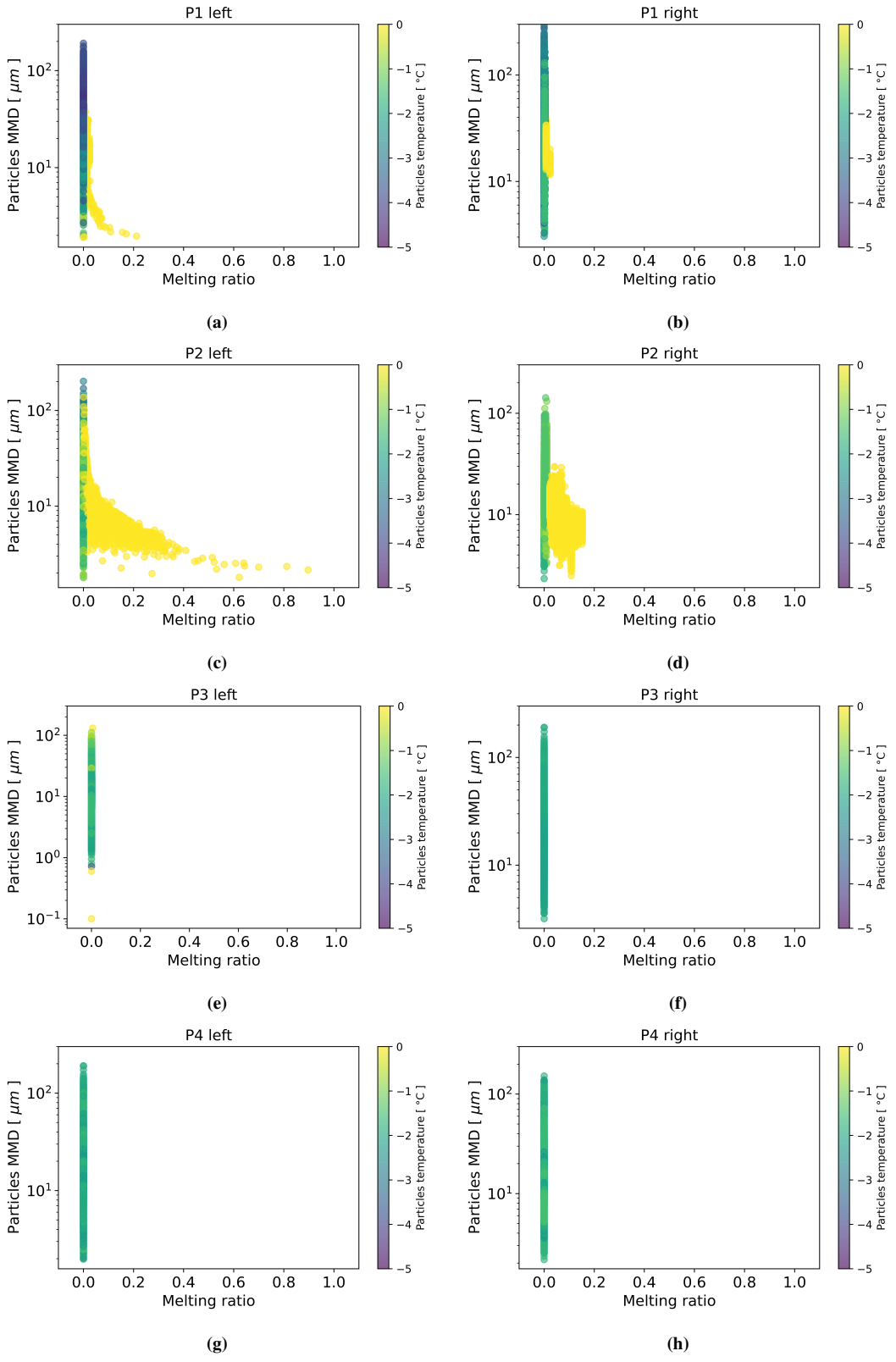

Fig. 16 Particles melting ratio with respect to particles MMD and particles temperature on upstream (left) and downstream (right) sides of mixing planes for Scan #132.01

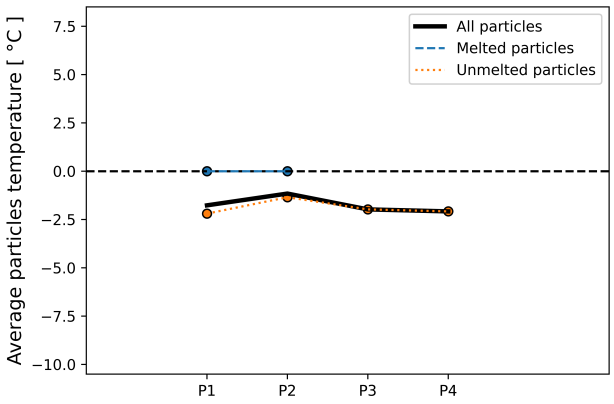

Fig. 17 Average particle temperature for Scan #132.01

before decreasing at plane P3. The temperature increase is globally related to the airflow's temperature rise at the rotor and stator level Figures 14b. In addition, since some particles are melted, the average temperature is biased toward the melting temperature of 0 °C. It is indeed clearly visible on Figure 17 showing the particle temperature at mixing planes' right side, as averaged, for melted particles, unmelted particles and all particles. Concerning the temperature decrease, it is attributed to evaporation/sublimation. Indeed, melted particles are subjected to evaporation/sublimation, deposition or solidification. The latter is dismissed since the air temperature does not decrease along the compressor, see Figure 14b, and the two-way coupling is not considered in this investigation (nevertheless, it has been tested and did not exhibit any significant impact on the results). The melted particles impinging upon walls tend to stick on it whereas particles far from the walls are subjected to evaporation/sublimation. Similarly unmelted particles could experience sublimation. This is shown in Figures 14l-14m where one can see a large amount of particles deposition and a small amount of particles evaporation/sublimation in the rotor level respectively. Conversely, in the stator level, a small amount of particles stick on walls whereas a large amount of particles experience evaporation/sublimation. These two thermodynamics processes are accompagnied by a strong decrease of particle temperature as was shown in [43].

Finally, it is worth pointing out the discrepancies on data transfer procedure at mixing planes. Considering Figure 15 (and also Figure 16), it is clear that the histogram of particles in the right plane differs from that in the left plane. These discrepancies are related to the mixing plane procedure, where only average particles characteristics are transferred from a module's exit to the next module's inlet. As a consequence, even if the average temperature is conserved, the melting ratio is highly reduced. This behavior finally leads to the inhibition of ice accretion in the test article.

XII. Conclusion

The present work deals with the numerical simulation of ice particle fragmentation, melting and accretion dynamics within the ICE-MACR single-stage compressor test rig.

Fragmentation dynamics were investigated for sufficiently cold conditions to inhibit melting totally, allowing the

study of the fragmentation effects separately from melting. Numerical simulations with two different fragmentation models denoted 'HAIC' and 'MUSIC-haic' were examined. It turns out that both models predict very similar fragment size distributions, both for the maximum fragment diameter and the fragment size distribution. Considering particle dynamics after fragmentation, only the predicted radial velocity component differs. Very similar characteristic diameters Dv10, Dv50 and Dv90 were observed for both models at the exit of the single compressor stage. A good agreement with experiments was obtained, especially at higher rotational speeds, i.e., 25 000 RPM and 33 000 RPM. At these higher speeds, most of the fragmentation is induced by particle impingement on the rotor, while impingement on the stator and outlet guide vanes (OGV) significantly contributes to the size reduction at lower rotational speeds (15 000 RPM). However, comparison of relative total water contents (TWC) over the radius between numerical simulations and experiments shows large discrepancies. Indeed, simulations predict a massive concentration at the casing downstream stage 1 while crystals are much more distributed along span in the experiment. The origin of these discrepancies is still unknown but is a matter of concern. Two distinct trajectory patterns were evidenced: centripetal trajectories for the ice particles impinging on the conical stator casing and centrifugal trajectories for those impinging on the spinner or rotor. It was also observed that these trajectories could cross at mixing plane locations. In such cases, defining the reinjection velocity as the average over all particles crossing a single ring is erroneous, and evaluating the influence of this error on results appears necessary.

In the second step, different operating points characterized by increasing static inlet air temperatures were simulated. They correspond to wet bulb temperatures increasing from negative to positive values and respectively exhibiting no accretion, significant accretion and moderate accretion. Additional fictitious intermediate operating points were also simulated to further assess melting and accretion sensitivity. The air temperature is overpredicted by up to 2 °C in the simulations compared to experimental data measured in the instrumentation vane, which should promote particle melting. However, the onset of melting is shifted towards even higher inlet air temperatures (+2 °C) in the numerical simulations. Nevertheless, once melting sets in, the sensitivity of melt ratio with respect to air inlet temperature variations is correctly reproduced, with 1 °C rise leading to 10% increase in melt ratio. The reasons for these discrepancies have been investigated. A deeper analysis of flow and particle properties along the rig has shown that partial melting starts in the rotor and stator modules. However numerical treatment at row interfaces leads to drastic reduction of those minority melted particles from upstream to downstream sides of mixing planes. Evaporation and sublimation contribute to make the remaining melted particles disappear, preventing any accretion from occurring in the test article. However, if the average inlet total temperature shift of about 2 °C is considered, the comparison of simulation results with experiments for the different operating points shows a good agreement in terms of occurrence, location and surfacic extension of accretion phenomena. In the computation process, the flowfield is not modified in order to take into account the change in flow path geometry due to ice shape, since this would imply to couple the accretion and gas flowfield solvers as well as the meshing. Extruding ice thickness in an unsteady process should then be inappropriate. While ice shapes do not

precisely align with experimental accretions, the severity (the potential threat to operability of an aircraft engine) were qualitatively matched for a high accretion case.

Acknowledgments

The funding received within the European Union's Horizon 2020 research and innovation programm under grant agreement No 767560 is gratefully acknowledged.

The authors thank Jennifer Chalmers from National Research Council of Canada who performed the particle sizing.

T. Soubrié thanks T. Herbez and J. Colomb for their contribution to the computations during their engineer internships.

References

[1] Yamazaki, M., Jemcov, A., and Sakaue, H., "A Review on the Current Status of Icing Physics and Mitigation in Aviation," *Aerospace*, Vol. 8, No. 7, 2021. doi:10.3390/aerospace8070188.

[2] Siquig, R. A., "Impact of Icing on Unmanned Aerial Vehicle (UAV) Operations," Tech. Rep. AD-A231 191, Naval Enironmental Prediction Research Facility, 1990.

[3] "Technical Compendium From Meetings of the Engine Harmonization Working Group," Tech. Rep. No. DOT/FAA/AR-09/13, FAA, March 2009.

[4] "In-Flight Icing Encounter and Loss of Control Simmons Airlines, d.b.a. American Eagle Flight 4184 Avions de Transport Regional (ATR) Model 72-212, N401AM, Roselawn, Indiana," Tech. rep., Aircraft Accident Report; National Transportation Safety Board, 1996.

[5] Cao, Y., Tan, W., and Wu, Z., "Aircraft Icing: an Ongoing Threat to Aviation Safety," *Aerospace Science and Technology*, Vol. 75, 2018, pp. 353–385. doi:10.1016/j.ast.2017.12.028.

[6] Currie, T. C., "Development of a Small Modular Multi-Stage Axial Compressor for Ice Crystal Icing Research," *AIAA AVIATION 2018 FORUM*, 2018. doi:10.2514/6.2018-4133.

[7] Neuteboom, M. O., Chalmers, J. L. Y., and Davison, C. R., "Ice Crystal Environment - Modular Axial Compressor Rig: Overview of Altitude Icing Commissioning," *AIAA AVIATION 2020 FORUM*, 2020. doi:10.2514/6.2020-2823.

[8] Chalmers, J., Wiebe, M., Neuteboom, M., and Davison, C., "Ice Crystal Environment Modular Axial Compressor Rig: Characterization of Particle Fracture and Melt across One Rotor Using Laser Shadowgraph," *AIAA AVIATION 2020 FORUM*, 2020. doi:10.2514/6.2020-2825.

[9] Davison, C., Chalmers, J., and Neuteboom, M., "Ice Crystal Environment-Modular Axial Compressor Rig: Evaluation of Measured Water Content and Melt," *AIAA AVIATION 2020 FORUM*, 2020. doi:10.2514/6.2020-2826.

[10] Chalmers, J., Cunnington-Bourbonniere, N., and Neuteboom, M., "Ice Crystal Environment Modular Axial Compressor Rig: Measurement of ice accretion from video," *AIAA AVIATION 2021 FORUM*, 2021. doi:10.2514/6.2021-2661.

[11] Neuteboom, M. O., Chalmers, J. L. Y., Mason, J., Chow, P., and Dumont, C., "Ice Crystal Environment - Modular Axial Compressor Rig: FAA 2021 Research Campaign," *AIAA AVIATION 2022 FORUM*, 2022. doi:10.2514/6.2022-3819.

[12] Nilamdeen, S., Shah, S., Stokes, J., Aliaga, C., Neuteboom, M. O., Chalmers, J. L. Y., Davison, C., and Fuleki, D., "Icing Simulation Studies on the NRC Rotating Rig," *AIAA AVIATION 2021 FORUM*, 2021. doi:10.2514/6.2021.

[13] Refloch, A., Courbet, B., Murrone, A., Villedieu, P., C, L., Gilbank, P., Troyes, J., Tessé, L., Chaineray, G., Dargaud, J.-B., Quémerais, E., and Vuillot, F., "CEDRE Software," *Aerospace Lab*, Vol. 2, 2011.

[14] Menter, F. R., "Improved two-equation k-omega turbulence models for aerodynamic flows," *Nasa Sti/recon Technical Report N*, Vol. 93, 1992, p. 22809.

[15] Osher, S., "Convergence of generalized MUSCL schemes," *SIAM Journal on Numerical Analysis*, Vol. 22, No. 5, 1985, pp. 947–961.

[16] Harten, A., Lax, P. D., and Leer, B. v., "On upstream differencing and Godunov-type schemes for hyperbolic conservation laws," *SIAM review*, Vol. 25, No. 1, 1983, pp. 35–61.

[17] Williams, F. A., "Spray combustion and atomization," *The physics of fluids*, Vol. 1, No. 6, 1958, pp. 541–545.

[18] Norde, E., Senoner, J.-M., van der Weide, E. T. A., Trontin, P., Hoeijmakers, H. W. M., and Villedieu, P., "Eulerian and Lagrangian ice-crystal trajectory simulations in a generic turbofan compressor," *Journal of Propulsion and Power*, Vol. 35, No. 1, 2019, pp. 26–40.

[19] Haselbacher, A., Najjar, F. M., and Ferry, J. P., "An efficient and robust particle-localization algorithm for unstructured grids," *Journal of Computational Physics*, Vol. 225, No. 2, 2007, pp. 2198–2213.

[20] Maxey, M. R., and Riley, J. J., "Equation of motion for a small rigid sphere in a nonuniform flow," *The Physics of Fluids*, Vol. 26, No. 4, 1983, pp. 883–889.

[21] Gatingol, R., "The Faxen formulae for a rigid particle in an unsteady non-uniform Stokes flow," *Journal de Mécanique Théorique et Appliquée*, Vol. 1, No. 2, 1983, pp. 143–160.

[22] Ganser, G. H., "A rational approach to drag prediction of spherical and nonspherical particles," *Powder technology*, Vol. 77, No. 2, 1993, pp. 143–152.

[23] Sirignano, W. A., and Edwards, C. F., "Fluid dynamics and transport of droplets and sprays," *Journal of Fluids Engineering*, Vol. 122, No. 1, 2000, pp. 189–190.

[24] Trontin, P., Blanchard, G., and Villedieu, P., "A comprehensive numerical model for mixed-phase and glaciated icing conditions," *8th AIAA Atmospheric and Space Environments Conference*, 2016, p. 3742.

[25] Senoner, J. M., Trontin, P., Reitter, L., Karpen, N., Schremb, M., Vargas, M., and Villedieu, P., "Ice particle impact on solid walls: size modeling of reemited fragments," *International Journal of Impact Engineering*, Vol. 160, 2022. doi: 10.1016/j.ijimpeng.2022.104322.

[26] Vidaurre, G., and Hallett, J., "Particle Impact and Breakup in Aircraft Measurement," *Journal of Atmospheric and Oceanic Technology*, Vol. 26, No. 5, 2015, pp. 972–983.

[27] Grady, D., "The spall strength of condensed matter," *Journal of the Mechanics and Physics of Solids*, Vol. 36, No. 3, 1988, pp. 353–384.

[28] Glenn, L., and Chudnovsky, A., "Strain-energy effects on dynamic fragmentation," *Journal of Applied Physics*, Vol. 59, No. 4, 1986, pp. 1379–1380.

[29] Hutchings, I., "Strain rate effects in microparticle impact," *Journal of Applied Physics*, Vol. 10, No. 14, 1977, p. L179.

[30] Roisman, I., and Tropea, C., "Impact of a crushing ice particle onto a dry solid wall," *Proceedings of the Royal Society A: Mathematical, Physical and Engineering Sciences*, Vol. 471, No. 2183, 2015, p. 20150525.

[31] Nelsen, R. B., *An introduction to copulas*, Springer Science & Business Media, 2007.

[32] Gomez de Segura Solay, G., Radenac, E., Chauvin, R., and Laurent, C., "Simulations of ice accretion, runback and droplet," *AIAA*, 2016.

[33] Trontin, P., and Villedieu, P., "A comprehensive accretion model for glaciated icing conditions," *International Journal of Multiphase Flow*, Vol. 108, 2018, pp. 105–123.

[34] Charton, V., "Modélisation de l'accrétion de glace dans les turboréacteurs en conditions cristaux," Ph.D. thesis, Université de Toulouse, 2020.

[35] Charton, V., Trontin, P., Aouizerate, G., and Villedieu, P., "Semi-Empirical Modelling of Erosion Phenomena for Ice Crystal Icing Numerical Simulation," *SAE International journal of advances and current practices in mobility*, Vol. 110, 2019.

[36] Finnie, I., and McFadden, D. H., "On the velocity dependence of the erosion of ductile metals by solid particles at low angles of incidence," *Wear*, Vol. 48, 1978, pp. 181–190.

[37] Bitter, J. G. A., "A study of erosion phenomena part i," *Wear*, Vol. 6, No. 11, 1963, pp. 5–21.

[38] Bitter, J. G. A., "A study of erosion phenomena part ii," *Wear*, Vol. 6, No. 13, 1963, pp. 169–190.

[39] Laurent, C., Bouyges, M., Bennani, L., Senoner, J. M., and Charton, V., "Ice crystals accretion capabilities of ONERA's 3D icing suite," *AIAA AVIATION 2022 FORUM*, 2022. doi:10.2514/6.2022-3537.

[40] Li, T., Li, S., Zhao, J., Lu, P., and Meng, L., "Sphericities of non-spherical objects," *Particuology*, Vol. 10, 2012, p. 97–104. doi:10.1016/j.partic.2011.07.005.

[41] Desjardins, O., Fox, R. O., and Villedieu, P., "A quadrature-based moment method for dilute fluid-particle flows," *Journal of Computational Physics*, Vol. 227, No. 4, 2008, pp. 2514–2539.

[42] Soubrié, T., Laurent, C., and Bouyges, M., "Ice accretion modelling in the ICE-MACR compressor rig," *AIAA AVIATION 2022 Forum*, 2022. doi:10.2514/6.2022-3536.

[43] Villedieu, P., Trontin, P., and Chauvin, R., "Glaciated and mixed phase ice accretion modeling using ONERA 2D icing suite," *6th AIAA Atmospheric and Space Environments Conference*, 2014. doi:10.2514/6.2014-2199, URL https://arc.aiaa.org/doi/abs/10.2514/6.2014-2199.